https://doi.org/10.5194/ms-2026-210
Preprint. Discussion started: 26 November 2026
© Author(s) 2026. CC BY 4.0 License.



mechanical sciences
DISCUSSIONS

Study on the Lubrication and Friction Reduction Characteristics of Textured Reciprocating Plunger Pairs

Tao He[1,2,3], Qiao Zhang[1], Yunlong Gu[1], Gang Luo[1,2], Kaiping Zhao[2], Chuanli Wang[1,2,3]

[1]School of Mechatronics Engineering, Anhui University of Science and Technology, Huainan Anhui 232001, China
[2]State Key Laboratory of Digital Intelligent Technology for Unmanned Coal Mining, Anhui University of Science and Technology, Huainan Anhui 232001, China
[3]Anhui Key Laboratory of Mine Intelligent Equipment and Technology, Anhui University of Science and Technology, Huainan Anhui 232001, China

Correspondence to: Chuanli Wang (chlwangaust@163.com)

Abstract. Horizontal plunger pumps are key power equipment in fully mechanized coal mining support systems, where piston pairs are prone to lubrication failure under extreme underground conditions. A hydrodynamic lubrication model of a textured piston pair was established using the finite difference method to investigate the effects of texture radius and depth on cyclic lubrication performance. Considering the periodic variation in the effective contact area, the piston stroke was divided into regions, and the effects of different texture-radius and texture-depth combinations were analyzed to identify favorable texture configurations and regional arrangements. Experimental tests were also conducted. The results show that lubrication performance is strongly affected by the texture-radius combination. The friction force of the large–small–large (DXD) configuration is generally lower than that of the small–large–small (XDX) configuration, while the maximum friction force and inflection points occur near the region boundaries. As the length of Region 2 increases, the maximum friction force decreases, its position shifts leftward, and the inflection-point region becomes longer, indicating that the friction force curve can be regulated by adjusting the position of Region 2. Experiments further show that the R3-2-3 combined texture provides the best friction-reduction performance, reducing the mean friction coefficient by 53.9% compared with the control group. These findings provide a basis for friction-reduction design of textured pistons in horizontal plunger pumps.

1 Introduction

Green and efficient coal mining is an important component of the energy system and an essential pathway for China's coal industry to achieve safe, efficient, and environmentally sustainable production as well as industrial transformation and upgrading. Owing to their simple structure, strong impact resistance, and capability for high-pressure operation, horizontal plunger pumps serve as core power components in fully mechanized coal mining support equipment (Liu et al., 2023; R. Li et al., 2024). However, owing to the harsh underground coal-mine environment, the piston pair undergoes reciprocating motion under extreme operating conditions characterized by high pressure, high flow rate, and severe contamination, making it prone to lubrication failure as well as friction and wear problems (Liang et al., 2026; Wang et al., 2024). This shortens the service

https://doi.org/10.5194/ms-2026-210
Preprint. Discussion started: 26 November 2026
© Author(s) 2026. CC BY 4.0 License.



mechanical sciences DISCUSSIONS

life of horizontal plunger pumps and compromises the safety of underground coal mining operations (Li, 2019; Zhang et al., 2021).

Surface texturing technology improves the lubrication performance of friction pairs by introducing regularly distributed textures on the contacting surfaces and has been widely applied in recent years to internal combustion engines (Liu et al., 2024; Pawlus and Reizer, 2022), gears (Liu et al., 2026), bearings (Yu et al., 2026; Wu et al., 2026), cutting tools (Niu et al., 2026; Zhu et al., 2026), nanogenerators (Yang et al., 2024), and friction-induced noise control (Qin et al., 2025). Mishra and Penchaliah (2021) investigated the effects of coatings and surface textures on the tribological performance of piston ring–cylinder liner pairs and found that textured coatings exhibited favorable friction-reduction performance. He et al. (2025) demonstrated that an appropriate texture arrangement could reduce abrasive wear in a reciprocating slider–wear-resistant sleeve friction pair. Gao et al. (2020, 2024) addressed the friction and wear problems of BW-250 mud pump pistons by designing a bionic piston with cylindrical dimple textures inspired by the surface morphology of earthworms. Experimental results showed that these textures reduced friction by storing lubricating medium and wear debris. Lu (2022) investigated the effects of texture parameters on the lubrication performance of piston pairs through experiments and simulations, and found that textured piston pairs exhibited higher peak pressure and oil-film load-carrying capacity than smooth piston pairs.

However, the texture morphology and parameters suitable for different friction pairs vary. Therefore, considerable attention has been given to the effects of texture morphology and structural parameters on lubrication performance. Ma et al. (2022) investigated the friction-reduction performance of sinusoidal textures with different spacings through experiments and simulations. The results showed that an appropriate texture spacing could enhance the local hydrodynamic effect and promote the formation of a tribofilm, thereby improving tribological performance through their synergistic action. X. Li et al. (2026) combined numerical simulations and experiments to investigate the lubrication performance of teardrop-shaped textures and found that texture shape, size, and spacing significantly affected the friction-reduction effect. Wang et al. (2018b) solved the Reynolds equation using the finite difference method and analyzed the oil-film thickness and pressure for spherical-cap, square, and cylindrical textures. They found that each texture morphology had a corresponding optimal parameter combination that provided the best lubrication condition for an axial piston pump. Cheng et al. (2023) and Zhang and Chen (2021) applied spherical-cap textures to internal combustion engine cylinder liners and three-oil-wedge hydrodynamic journal bearings, respectively, and investigated their effects on lubrication performance through friction and wear tests, flow-field analysis, and Reynolds equation solutions. Luo et al. (2025) established a low-pressure-stroke lubrication model for a textured piston pair in an axial piston pump and analyzed the effects of texture parameters on lubrication characteristics. These studies indicate that an appropriate arrangement of spherical-cap textures and optimization of their structural parameters can improve the load-carrying capacity, lubrication performance, and operational stability of friction pairs.

In addition to texture morphology and parameters, the arrangement of textures also affects the lubrication performance of friction pairs. Y. Li et al. (2024) optimized the texture distribution based on a mass-conserving cavitation boundary condition. The results showed that an appropriate asymmetric texture arrangement could generate a continuous high-pressure region through the collective effect of the textures, thereby improving the oil-film load-carrying capacity. Fan et al. (2023) introduced

https://doi.org/10.5194/ms-2026-210
Preprint. Discussion started: 26 November 2026
© Author(s) 2026. CC BY 4.0 License.



mechanical sciences DISCUSSIONS

combined textures consisting of spherical-cap and sinusoidal dimples in the hydrodynamically lubricated region of an internal combustion engine cylinder liner. Wang et al. (2023) investigated the effects of different arrangements of combined textures on bearing lubrication characteristics. Both studies showed that, under hydrodynamic lubrication conditions, friction pairs with combined textures exhibited better friction-reduction performance than those with a single texture. He et al. (2021, 2026) investigated the effects of texture arrangement, size, shape, and spacing on friction-pair performance from the perspectives of load-carrying characteristics and friction and wear behavior. The results indicated that appropriate texture combinations could improve the lubrication, load-carrying, and friction-reduction performance of friction pairs.

Regarding numerical methods, Wang et al. (2018a) solved the oil-film pressure in the valve-plate pair of a piston pump using the finite difference method combined with a relaxation iteration scheme. Profito et al. (2024) validated the effectiveness of numerical analysis for textured lubrication through a Reynolds-based model and friction experiments.

The above studies indicate that surface texturing can effectively improve the lubrication and friction-reduction performance of friction pairs, and its effectiveness is influenced by texture morphology, structural parameters, and arrangement. However, the contact area between the piston and the wear-resistant ring varies periodically with piston motion, resulting in a contact configuration that differs from that of conventional reciprocating friction pairs. Therefore, existing findings on surface texturing cannot be directly applied to this type of piston pair.

Based on the operating principle of a horizontal plunger pump, a kinematic model of the piston pair was established and its governing equations of motion were derived. Combined with hydrodynamic lubrication theory, a hydrodynamic lubrication model of the textured piston pair was developed using spherical-cap textures. The lubrication model was discretized and solved using the finite difference method to investigate the effects of texture radius, texture depth, and texture arrangement on the lubrication characteristics of the piston pair. On this basis, reciprocating friction and wear tests were designed and conducted to validate the simulation results. The findings provide a basis for the friction-reduction design of textured pistons in horizontal plunger pumps.

2 Hydrodynamic Lubrication Model of a Textured Piston Pair

2.1 Kinematic Analysis of the Piston Pair

Figure 1 shows schematic diagrams of the piston-pair motion and lubrication model. Figure 1(a) shows the reciprocating motion of the piston. O is the center of rotation of the crankshaft, l_1 is the crank eccentricity, l_2 is the connecting-rod length, θ is the crank angle, and β is the connecting-rod angle. Let $\delta=l_1/l_2$. When the crankshaft rotates at an angular velocity of ω, the crank angle at time t is given by $\theta=\omega t$.

Accordingly, the piston displacement s can be obtained. Differentiating the piston displacement with respect to time t gives the piston velocity v_p:

$$s = l_1(1-cos\theta) + l_2(1- \sqrt{1-\delta^2 sin^2\theta}), \quad (1)$$

https://doi.org/10.5194/ms-2026-210
Preprint. Discussion started: 26 November 2026
© Author(s) 2026. CC BY 4.0 License.



mechanical sciences DISCUSSIONS

$$v_p = \frac{ds}{dt} = l_1\omega(sin\theta + \frac{\delta}{2}\frac{sin2\theta}{\sqrt{1-\delta^2 sin^2\theta}}), \quad (2)$$

For computational convenience while maintaining sufficient accuracy, the displacement and velocity expressions were expanded to second order, with higher-order terms neglected (Wang et al., 2019). The resulting expressions are:

$$s = l_1(1 - cos\theta) + \frac{\delta}{4}l_1(1 - cos2\theta), \quad (3)$$

$$v_p = l_1\omega(sin\theta + \frac{\delta}{2}sin2\theta), \quad (4)$$

2.2 Dynamic Contact Lubrication Analysis of the Piston Pair

To evaluate the lubrication performance of the piston pair, its motion state was analyzed using the piston motion equations. Figure 1(b) shows the dynamic contact between the piston and the wear-resistant ring, where the contact region varies with piston velocity. The contact region is defined as the computational region, with the regions to its left and right defined as the uncalculated and calculated regions, respectively. Thirty velocity points during the fluid discharge process were selected for numerical calculation.

2.3 Hydrodynamic Lubrication Model of the Textured Piston Pair

The Reynolds equation is derived from the Navier–Stokes and continuity equations under the assumptions of Newtonian, predominantly laminar flow, no slip, negligible gravity and inertia, negligible pressure variation across the oil-film thickness, and constant viscosity along the film-thickness direction. Based on these assumptions, a differential element is selected from the piston-pair oil film, with an arbitrary point denoted as $(\tilde{x}, \tilde{y})$. As shown in Fig. 1(c), the oil-film pressure equation for the textured piston pair is derived as follows:

$$\frac{\partial}{\partial\tilde{x}}(\frac{h^3}{\eta}\frac{\partial p}{\partial\tilde{x}}) + \frac{\partial}{\partial\tilde{y}}(\frac{h^3}{\eta}\frac{\partial p}{\partial\tilde{y}}) = 6v_p\frac{\partial h}{\partial\tilde{y}}, \quad (5)$$

where p denotes the fluid pressure, η denotes the dynamic viscosity, and h denotes the oil-film thickness.

2.4 Oil-Film Thickness Equation

As illustrated in Fig. 1(c), the oil-film thickness h consists of the clearance film thickness h_0 of the piston pair and the texture-induced film thickness h_m. Γ denotes the textured region.

$$h(\tilde{x}, \tilde{y}) = \begin{cases} h_0 + h_m & (\tilde{x}, \tilde{y}) \in \Gamma \\ h_0 & (\tilde{x}, \tilde{y}) \notin \Gamma \end{cases}, \quad (6)$$

The textured surface of the piston is divided into $N \times M$ texture units, with each texture dimple located at the center of a texture unit. A local coordinate system, denoted by $(\tilde{x}_1\tilde{o}_1\tilde{y}_1)$, is defined for each texture unit and satisfies the following relationship:

https://doi.org/10.5194/ms-2026-210
Preprint. Discussion started: 26 November 2026
© Author(s) 2026. CC BY 4.0 License.



mechanical sciences DISCUSSIONS

$$\begin{cases} \tilde{x}_1 = \tilde{x} - L_c(n-1) \\ \tilde{y}_1 = \tilde{y} - L_c(m-1) \end{cases}, \tag{7}$$

where n = 1-N, m = 1-M, (n,m) denotes the row and column indices of a texture unit within the textured region, and L_c is the side length of the texture unit.

The radius of the circular opening of the spherical-cap texture is defined as the texture radius r_t. Point C is the center of the sphere, and CF, CQ and CK are all equal to the sphere radius R_t. In triangles ΔCDK and ΔCEQ, DK represents the texture radius r_t, DF represents the texture depth h_t, and GQ represents the texture-induced film thickness h_m. Based on the geometric relationships between the side lengths of the triangles, the profile equation of the spherical-cap texture is derived as follows:

$$h_m = \sqrt{R_t^2 - ((\tilde{x}_1 - L_c/2)^2 + (\tilde{y}_1 - L_c/2)^2)} - (R_t - h_t), \tag{8}$$

where $R_t = (r_t^2 + h_t^2)/(2h_t)$.

3 Model Solution

3.1 Numerical Solution of Oil-Film Pressur

Figure 1(d) shows a schematic diagram of the computational-domain mesh. The computational domain in the $\tilde{x}\tilde{o}\tilde{y}$ plane is divided into a uniform grid, with a total of $I \times J$ nodes in the $\tilde{x}$ and $\tilde{y}$ directions. The position of each node in the computational domain is denoted by (i, j), and the grid spacings in the$\tilde{x}$ and $\tilde{y}$ directions are $\Delta\tilde{x}$ and $\Delta\tilde{y}$, respectively.

Equation (5) is discretized using the central difference scheme of the finite difference method. The partial derivatives of the pressure $p(i, j)$ at an arbitrary node within the computational domain are expressed in terms of the pressures at its four neighboring nodes (Huang, 2013). The central difference formulas are given as follows:

$$\begin{cases} \left(\frac{\partial p}{\partial \tilde{x}}\right)_{i,j} = \frac{p_{i+1,j} - p_{i-1,j}}{2\Delta\tilde{x}} \\ \left(\frac{\partial p}{\partial \tilde{y}}\right)_{i,j} = \frac{p_{i,j+1} - p_{i,j-1}}{2\Delta\tilde{y}} \end{cases}, \tag{9}$$

$$\begin{cases} \left(\frac{\partial^2 p}{\partial \tilde{x}^2}\right)_{i,j} = \frac{p_{i+1,j} + p_{i-1,j} - 2p_{i,j}}{(\Delta\tilde{x})^2} \\ \left(\frac{\partial^2 p}{\partial \tilde{y}^2}\right)_{i,j} = \frac{p_{i,j+1} + p_{i,j-1} - 2p_{i,j}}{(\Delta\tilde{y})^2} \end{cases}, \tag{10}$$

https://doi.org/10.5194/ms-2026-210
Preprint. Discussion started: 26 November 2026
© Author(s) 2026. CC BY 4.0 License.

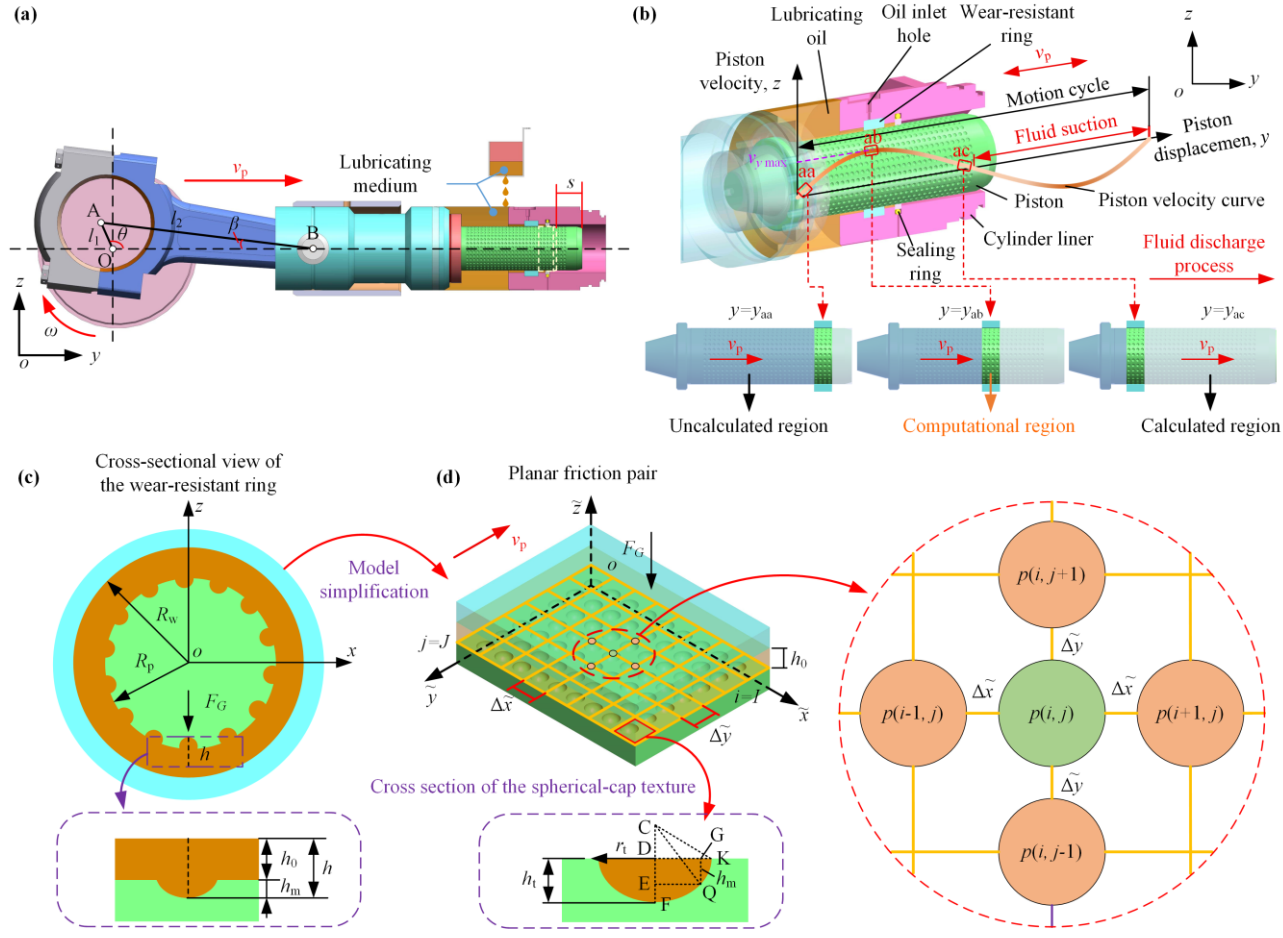


Figure 1. Schematic diagrams of piston-pair motion and lubrication model: (a) piston reciprocating motion; (b) dynamic contact of the piston pair; (c) simplified model of the piston pair; (d) computational-domain meshing

According to the central difference formulas, the partial derivatives are replaced by difference quotients, yielding the following relationship between the pressure pi,j at each node and the pressures at its neighboring nodes:

$$p_{i,j} = C_A p_{i+1,j} + C_B p_{i-1,j} + C_C p_{i,j+1} + C_D p_{i,j-1} + C_E, \quad (11)$$

where C_A, C_B, C_C, C_D and C_E are known coefficients.

Equation (11) gives one pressure equation per node, forming a system of linear algebraic equations. With the computational region boundary conditions, this system is solved using a direct iterative method to obtain the oil-film pressure distribution. Because varying equation residuals prevent direct assessment of absolute accuracy, a relative convergence criterion is adopted: iteration stops when the relative pressure difference E_p between successive iterations satisfies the prescribed pressure convergence tolerance ε_p, where k denotes the iteration number.

https://doi.org/10.5194/ms-2026-210
Preprint. Discussion started: 26 November 2026
© Author(s) 2026. CC BY 4.0 License.



mechanical sciences DISCUSSIONS

$$\frac{\sum_{I}^{i=1}\sum_{J}^{j=1}|p_{i,j}^{k}-p_{i,j}^{k-1}|}{\sum_{I}^{i=1}\sum_{J}^{j=1}|p_{i,j}^{k}|}=E_p\le\epsilon_p, \tag{12}$$

Since the load-carrying capacity $F_{\tilde{z}}$ provided by the oil film may not necessarily balance the radial load F_G, a load-balance condition is introduced to correct the clearance film thickness h_0 between the piston and the wear-resistant ring. The load-balance condition is given by:

$$\frac{|F_G-F_{\tilde{z}}|}{F_{\tilde{z}}}=E_F\le\epsilon_F, \tag{13}$$

where ϵ_F is the load convergence tolerance and E_F is the relative load difference.

The clearance film thickness h_0^k at the kth iteration is corrected using the relaxation factor ξ and the initial clearance film thickness h_p:

$$\begin{cases} h_0^k=h_0^{k-1}+\xi h_p & F_G<F_{\tilde{z}} \\ h_0^k=h_0^{k-1}-\xi h_p & F_G>F_{\tilde{z}}' \end{cases} \tag{14}$$

3.2 Oil-Film Load-Carrying Capacity and Friction Force

From differential-element force equilibrium and Newton's law of viscosity, the friction force $F_{\tilde{y}}$ on the piston surface is:

$$F_{\tilde{y}}=\int\int\left(-\frac{h}{2}\frac{\partial p}{\partial\tilde{y}}+\frac{v_p\eta}{h}\right)d\tilde{x}d\tilde{y}, \tag{15}$$

During piston reciprocation, the friction coefficient f is calculated using the radial load F_G of the piston pair as:

$$f=\frac{F_{\tilde{y}}}{F_G}, \tag{16}$$

The oil-film load-carrying capacity $F_{\tilde{z}}$ is given by:

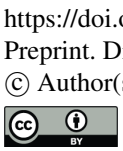
$$F_{\tilde{z}}=\int\int p(\tilde{x},\tilde{y})d\tilde{x}d\tilde{y}, \tag{17}$$

The leakage flow rate q of the lubricating medium through the oil-film boundary is:

$$q=\int\left(-\frac{h^3}{12\eta}\frac{\partial p}{\partial\tilde{y}}+v_p\frac{h}{2}\right)d\tilde{y}, \tag{18}$$

Figure 2 shows the numerical calculation flowchart for hydrodynamic lubrication of the piston pair. The computational region and mesh are first determined from the lubricating oil, operating and geometric parameters. A texture morphology model is then established, and the oil-film pressure is solved iteratively using the finite difference method. After pressure convergence, the oil-film load-carrying capacity is calculated and compared with the external load. Once the specified convergence tolerance is satisfied, the converged pressure is used to calculate the friction force, friction coefficient and leakage flow rate.

https://doi.org/10.5194/ms-2026-210
Preprint. Discussion started: 26 November 2026
© Author(s) 2026. CC BY 4.0 License.



mechanical sciences
DISCUSSIONS

3.3 Numerical Program Validation

Simulations were performed using the same texture parameters, mesh parameters, lubricant viscosity and velocity as those reported by Bao et al. (2019). The side length of the texture unit was L_c=0.5 mm, the circular texture radius was r_t=100 μm, the clearance film thickness of the friction pair was h_0=5 μm, the texture dimple depth was h_t=10 μm, the lubricant viscosity was η_0=0.09845 Pa·s, and the relative sliding velocity of the friction pair was v_p=0.625 m/s. Table 1 compares the calculation results for the texture unit. The friction force agrees well with that reported by Bao et al. (2019), with relative errors of approximately 1% in the load-carrying capacity and friction coefficient. These results demonstrate the reliability of the numerical program for the hydrodynamic lubrication model of the textured piston pair.

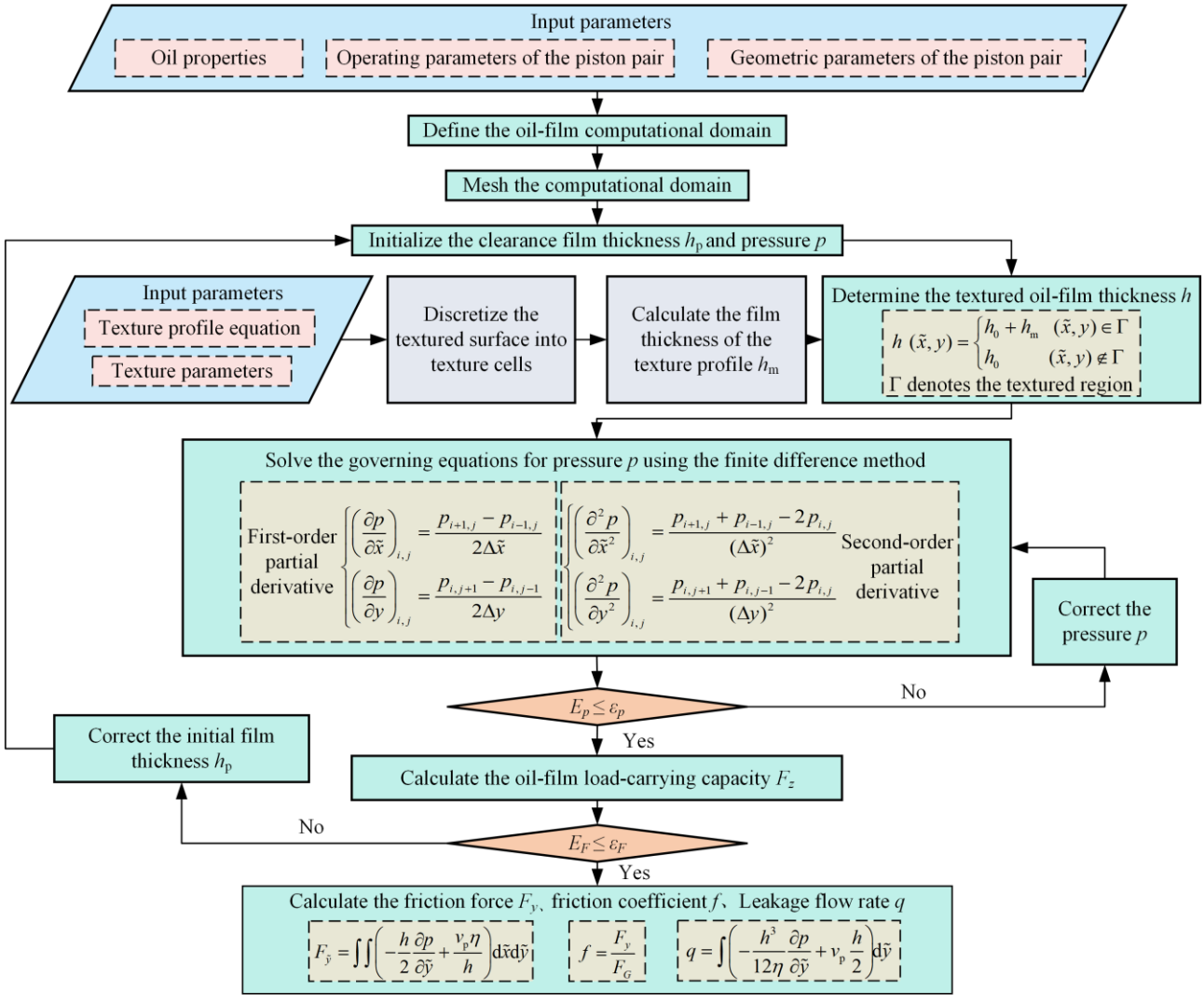


Figure 2. Numerical calculation flowchart for the hydrodynamic lubrication of the textured piston pair.

Table 1. Comparison of calculation results for the texture unit.

https://doi.org/10.5194/ms-2026-210
Preprint. Discussion started: 26 November 2026
© Author(s) 2026. CC BY 4.0 License.



mechanical sciences DISCUSSIONS

	Load-carrying capacity (N)	Friction force (N)	Friction coefficient
Present calculation	0.0274	0.0028053	0.10235
Reference calculation	0.0277	0.0027966	0.10119
Relative error	1.1%	0.3%	1.1%

3.4 Boundary Conditions and Grid Independence Verification

The Reynolds cavitation boundary condition was adopted for the lubrication calculation of the piston pair. When solving the differential equations for pressure, pressure values lower than the cavitation pressure p_c were set equal to the cavitation pressure. The radial load was set to 20 N, and the remaining calculation parameters are listed in Table 2.

Table 2. Lubrication calculation parameters of the piston pair.

Parameter	Value	Parameter	Value
Inlet pressure $p_{j=1}$/MPa	0.1	Pressure convergence tolerance ε_p/-	5×10^{-5}
Outlet pressure $p_{j=J}$/MPa	0.1	Load convergence tolerance ε_F/-	10^{-2}
Ambient-pressure viscosity η_0/(Pa·s)	0.05	Cavitation pressure (Liu, 2013) p_c/MPa	10^{-8}
Piston displacement s/mm	50	Crankshaft speed n/r·min^{-1}	547
Crank eccentricity l_1/mm	25	Connecting-rod length l_2/mm	133

To ensure the accuracy of the calculation results, a grid independence verification was performed. The texture radius was set to r_t=400 μm, the texture dimple depth to h_t=20 μm, the computational domain size to 18 mm×18 mm, and the relative sliding velocity of the friction pair to v_p=1 m/s. Fig. 3 shows the friction coefficient of the friction pair obtained with different grid resolutions. The friction coefficient stabilizes when the grid resolution reaches 1080×1080. Therefore, a grid resolution of 1080×1080 was selected to ensure sufficient computational accuracy.

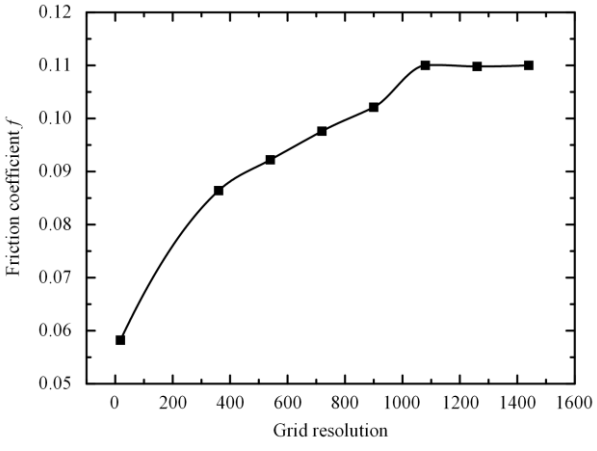


Figure 3. Grid independence verification

https://doi.org/10.5194/ms-2026-210
Preprint. Discussion started: 26 November 2026
© Author(s) 2026. CC BY 4.0 License.



mechanical sciences
DISCUSSIONS

4 Effects of Texture Geometric Parameters on Lubrication Characteristics

4.1 Effect of Texture Radius

Spherical-cap textures with radii of 400, 450, 500, 550, and 600 μm and a constant depth of 20 μm were simulated on the piston surface. As shown in Fig. 4, the hydrodynamic wedge effect generates high- and low-pressure regions in the converging and diverging wedges of each texture unit, respectively. Both the high- and low-pressure core regions expand with increasing texture radius.

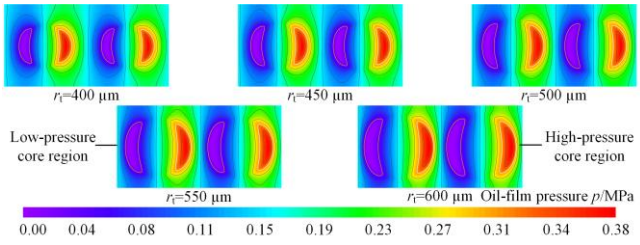


Figure 4. Local pressure contours under different texture radii.

Figure 5 shows the effects of texture radius on the lubrication characteristics of the piston pair. As shown in Fig. 5(a), the low-pressure region reaches the prescribed cavitation pressure, and the cavitation region widens with increasing texture radius. Once the cavitation pressure is reached, the oil-film pressure no longer decreases (Wang et al., 2025). Consequently, the depressed low-pressure area is smaller than the elevated high-pressure area, indicating a higher oil-film load-carrying capacity of the textured surface than the smooth surface.

In Fig. 5(b), the friction force follows the piston velocity, first increasing and then decreasing, with both reaching their peaks simultaneously. The friction force decreases with increasing texture radius and is lowest at 600 μm. The maximum friction forces for increasing texture radii are 2.45 N, 2.21 N, 2.02 N, 1.84 N, and 1.69 N, respectively. This decrease mainly results from enhanced cavitation-induced load-carrying and hydrodynamic lubrication effects.

Figure 5(c) shows that the clearance film thickness increases with increasing texture radius, reaching a maximum of 9.18 μm at 600 μm under the simulated operating conditions. Increasing the texture radius enhances the oil-film load-carrying capacity. With a constant external load, the clearance film thickness therefore increases to satisfy the load-balance condition, improving the lubrication performance of the piston pair.

Figure 5(d) shows that, over the half-cycle, increasing texture radius decreases the mean friction force and increases the mean leakage flow rate. At 400 μm, the mean friction force is highest at 2.17 N, while the mean leakage flow rate is lowest at 3.92 $mL \cdot min^{-1}$. At 600 μm, they reach their minimum of 1.46 N and maximum of 5.08 $mL \cdot min^{-1}$, respectively.

https://doi.org/10.5194/ms-2026-210
Preprint. Discussion started: 26 November 2026
© Author(s) 2026. CC BY 4.0 License.

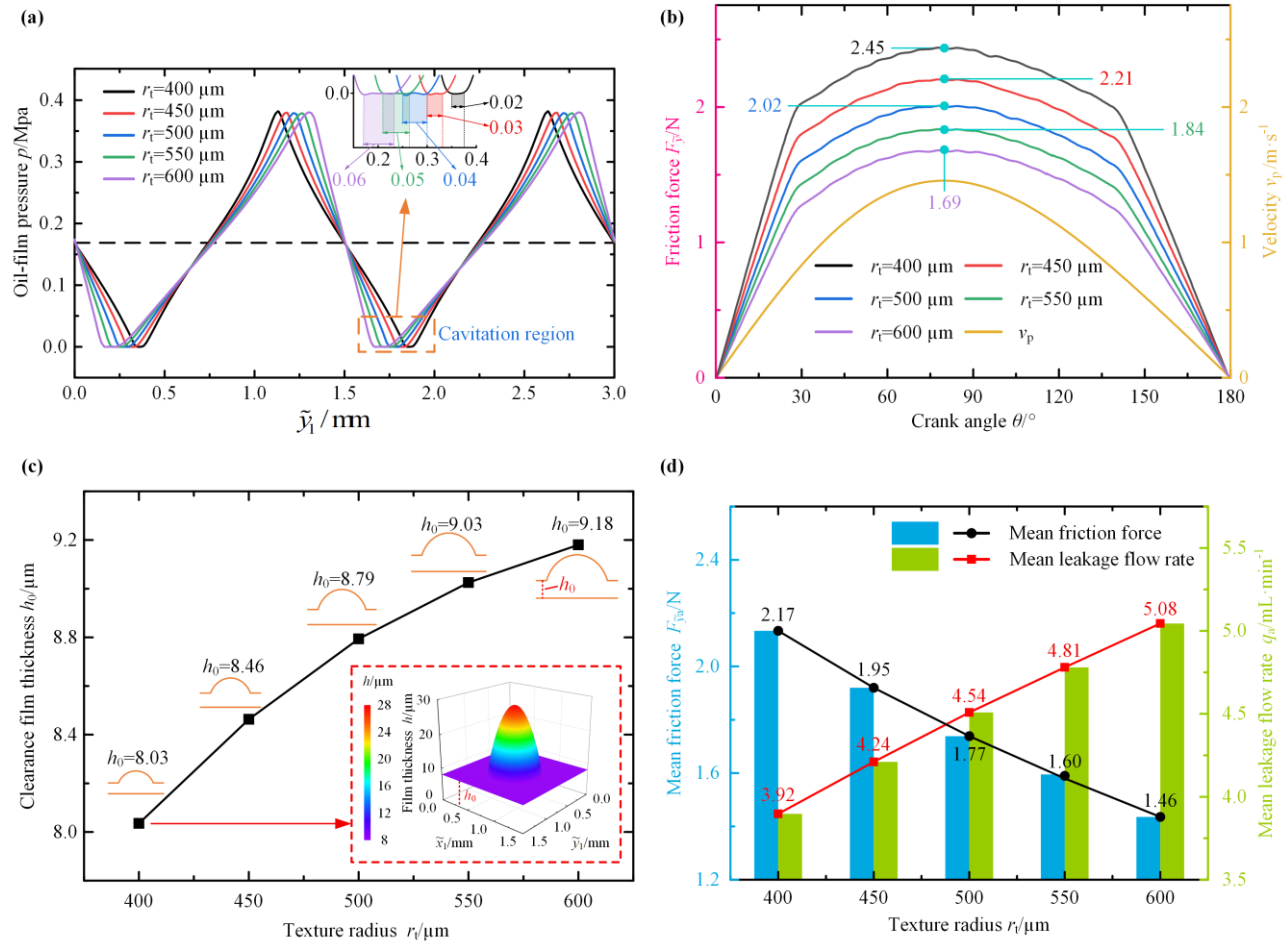


Figure 5. Effects of texture radius on the lubrication characteristics of the piston pair: (a) pressure distribution curves along the central cross-section under different texture radii; (b) friction force under different texture radii; (c) clearance film thickness under different texture radii; (d) mean friction force and mean leakage flow rate under different texture radii.

4.2 Effect of Texture Depth

Spherical-cap textures with depths of 20, 25, 30, 35, and 40 μm and a constant radius of 500 μm were simulated on the piston surface. As shown in Fig. 6, both the high- and low-pressure core regions shrink and gradually change from semicircular to crescent-shaped with increasing texture depth. At a texture depth of 40 μm, the difference in size between the two regions becomes particularly pronounced.

https://doi.org/10.5194/ms-2026-210
Preprint. Discussion started: 26 November 2026
© Author(s) 2026. CC BY 4.0 License.

mechanical sciences
DISCUSSIONS

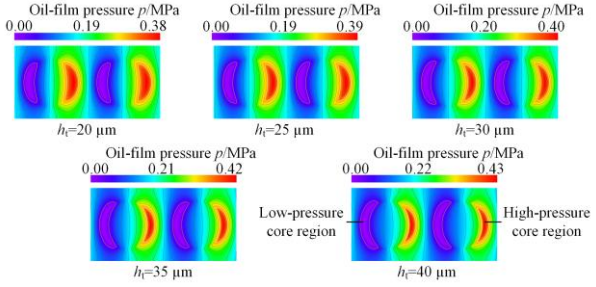


Figure 6. Local pressure contours under different texture depths.

Figure 7 shows the effects of texture depth on the lubrication characteristics of the piston pair. As shown in Fig. 7(a), the low-pressure regions along the central cross-section reach the prescribed cavitation pressure. Increasing texture depth shifts the
235 cavitation region slightly leftward and slightly increases the distance between the high- and low-pressure peaks.

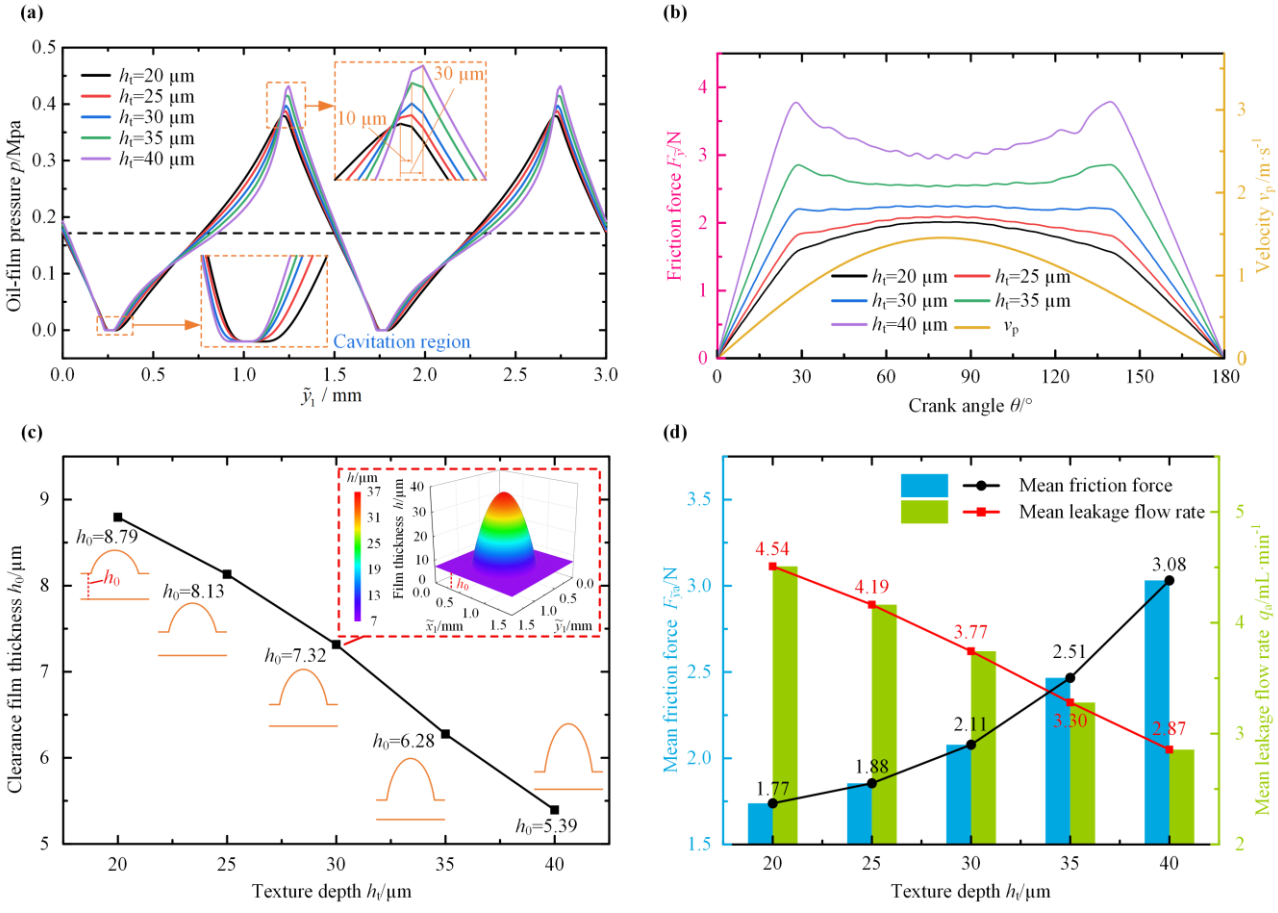


Figure 7. Effects of texture depth on the lubrication characteristics of the piston pair: (a) pressure distribution curves along the central cross-section under different texture depths; (b) friction force under different texture depths; (c) clearance film thickness under different texture depths; (d) mean friction force and mean leakage flow rate under different texture depths.

https://doi.org/10.5194/ms-2026-210
Preprint. Discussion started: 26 November 2026
© Author(s) 2026. CC BY 4.0 License.



mechanical sciences DISCUSSIONS

In Fig. 7(b), the friction force generally increases with texture depth, possibly because deeper textures promote oil entrapment and vortex dissipation, weakening the hydrodynamic effect and reducing lubrication performance (Yin et al., 2026). Equations (5) and (6) indicate that lubrication performance depends jointly on texture depth and piston velocity. Beyond a certain texture depth, piston velocity becomes dominant: increasing velocity enhances the hydrodynamic effect and oil-film load-carrying capacity, reducing friction force. Consequently, the friction force is higher at both ends of the half-cycle and lower in the middle.

In Fig. 7(c), the clearance film thickness decreases with increasing texture depth, reaching a minimum of 5.39 μm at 40 μm under the simulated operating conditions. This suggests deteriorating lubrication performance of the piston pair, consistent with Fig. 7(a).

Fig. 7(d) shows that increasing texture depth increases the mean friction force and decreases the mean leakage flow rate. At 20 μm, the mean friction force is lowest at 1.77 N, while the mean leakage flow rate is highest at 4.54 mL·min^{-1}. At 40 μm, they reach their maximum of 3.08 N and minimum of 2.87 mL·min^{-1}, respectively.

5 Effects of Texture Combination on Lubrication Characteristics

5.1 Design of Texture Combinations

Based on the preceding simulations, textures with radii of 500, 600, and 700 μm and textures with depths of 10, 15, and 20 μm were combined separately, as shown in Fig. 8.

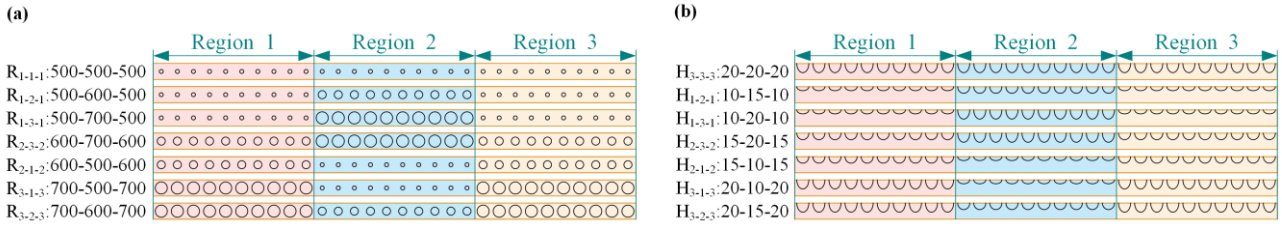


Figure 8. Design of texture combinations: (a) texture-radius combinations; (b) texture-depth combinations.

The preceding analysis suggests that, under the simulated operating conditions, increasing texture depth may reduce the oil-film load-carrying capacity and consequently increase the friction force. Lower texture depths were therefore selected to investigate how texture combinations affect the lubrication performance of the piston pair.

The piston pair exhibits different friction characteristics at low and high speeds. Considering manufacturability and computational complexity, the piston surface was divided along the stroke into three equal-length regions (Regions 1–3). As shown in Fig. 8(a), XDX denotes smaller texture radii in Regions 1 and 3 than in Region 2, whereas DXD denotes larger texture radii in Regions 1 and 3. Similarly, as shown in Fig. 8(b), QSQ denotes shallower texture depths in Regions 1 and 3 than in Region 2, whereas SQS denotes deeper texture depths in Regions 1 and 3. The three positions in each code correspond to Regions 1–3: R1, R2, and R3 denote texture radii of 500, 600, and 700 μm, respectively; H1, H2, and H3 denote texture

https://doi.org/10.5194/ms-2026-210
Preprint. Discussion started: 26 November 2026
© Author(s) 2026. CC BY 4.0 License.



mechanical sciences DISCUSSIONS

depths of 10, 15, and 20 μm, respectively. The uniform control (texture radius of 500 μm and texture depth of 20 μm) is coded $R_{1\text{-}1\text{-}1}$ for the texture-radius combinations and $H_{3\text{-}3\text{-}3}$ for the texture-depth combinations.

5.2 Effect of Texture-Radius Combination

For the XDX texture combinations, Fig. 9(a) and Fig. 9(b) show the friction force and leakage flow rate, respectively. Over the half-cycle, the friction force generally follows piston velocity, first increasing and then decreasing, with a V-shaped depression near the boundary between Regions 2 and 3. Friction-reduction performance ranks $R_{2\text{-}3\text{-}2}$, $R_{1\text{-}3\text{-}1}$, $R_{1\text{-}2\text{-}1}$, and $R_{1\text{-}1\text{-}1}$ from best to worst; the first three yield lower friction forces than the control group (R1-1-1). As the computational region enters Region 2, the increasing number of larger-radius texture units reduces the friction force. A greater difference in texture radius between Region 2 and the other regions produces greater friction reduction, consistent with the effect of increasing texture radius in Fig. 5(b).

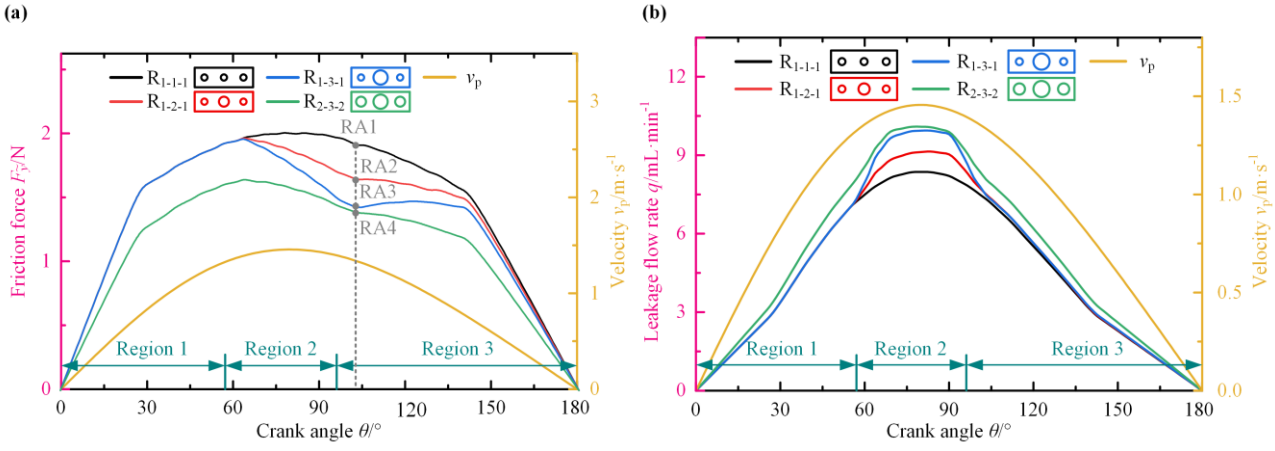
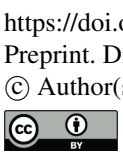


Figure 9. Friction force and leakage flow rate for XDX texture combinations: (a) friction force; (b) leakage flow rate.

In Fig. 9(a), the friction force inflection points occur slightly after the region boundaries where the texture radius changes, possibly because the friction force depends on the entire computational region and piston velocity. Upon entering Region 2, the computational region contains only a few larger-radius texture units, limiting their immediate effect on the overall friction force. As their number increases, their influence combines with piston velocity variation to produce an inflection point slightly after the boundary between Region 1 and Region 2, followed by decreasing friction force. Similarly, the increasing number of smaller-radius texture units in Region 3 produces another inflection point slightly after the region boundary, followed by increasing friction force.

Figure 10 presents the pressure contours at characteristic points RA1–RA4 for the XDX texture combinations. From RA1 to RA3, the maximum oil-film pressure increases with texture radius in Region 2, while the high- and medium-pressure regions remain nearly unchanged. The low-pressure region expands, but cavitation prevents further pressure reduction. Equation (17)

https://doi.org/10.5194/ms-2026-210
Preprint. Discussion started: 26 November 2026
© Author(s) 2026. CC BY 4.0 License.



mechanical sciences
DISCUSSIONS

defines the oil-film load-carrying capacity as the pressure integral over the effective load-carrying area; thus, it may increase with texture radius in Region 2 at RA1–RA3, consistent with Fig. 9(a).

As shown in Fig. 10, the maximum oil-film pressure at RA4 is slightly lower than that at RA3, but the medium- and high-pressure regions are larger, suggesting a higher oil-film load-carrying capacity.

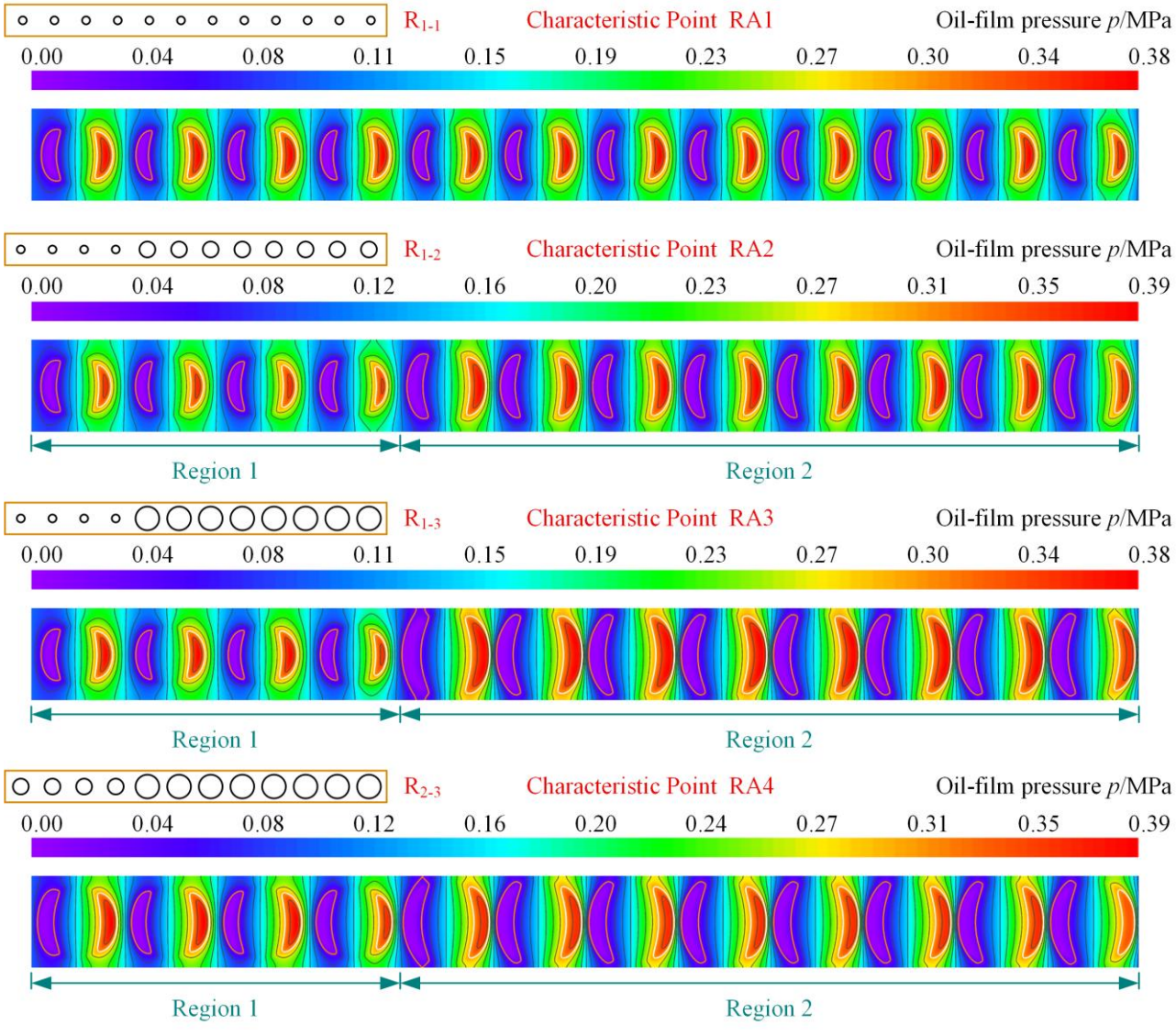
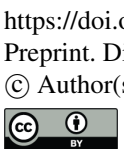


Figure 10. Pressure contours at characteristic points of the friction force curves for XDX texture combinations.

In Fig. 9(b), the leakage flow rate generally follows piston velocity over the half-cycle, first increasing and then decreasing, with a marked increase in Region 2.

In XDX, larger-radius textures occupy Region 2, while smaller-radius textures occupy Region 1 and Region 3. Under the simulated operating conditions, increasing texture radius in uniform textures enhances the overall oil-film load-carrying

https://doi.org/10.5194/ms-2026-210
Preprint. Discussion started: 26 November 2026
© Author(s) 2026. CC BY 4.0 License.



mechanical sciences DISCUSSIONS

capacity. Under a constant external load, the resulting increase in clearance film thickness reduces the friction force but increases the leakage flow rate, consistent with Fig. 5. A greater texture radius difference between Region 2 and the other regions amplifies both the reduction in friction force and the increase in leakage flow rate.

Figure 11 shows the friction force and leakage flow rate for the DXD texture combinations. Fig. 11(a) presents the friction force, whereas Fig. 11(b) presents the leakage flow rate. All DXD combinations yield lower friction forces than the control group. As shown in Fig. 9(a), the overall friction-force trends and inflection-point positions of the XDX combinations are similar to those of the DXD combinations. As the computational region enters Region 2, the increasing number of smaller-radius texture units raises the friction force; as it enters Region 3, the increasing number of larger-radius units lowers it. This regional trend is opposite to that of XDX, although the underlying mechanism is similar.

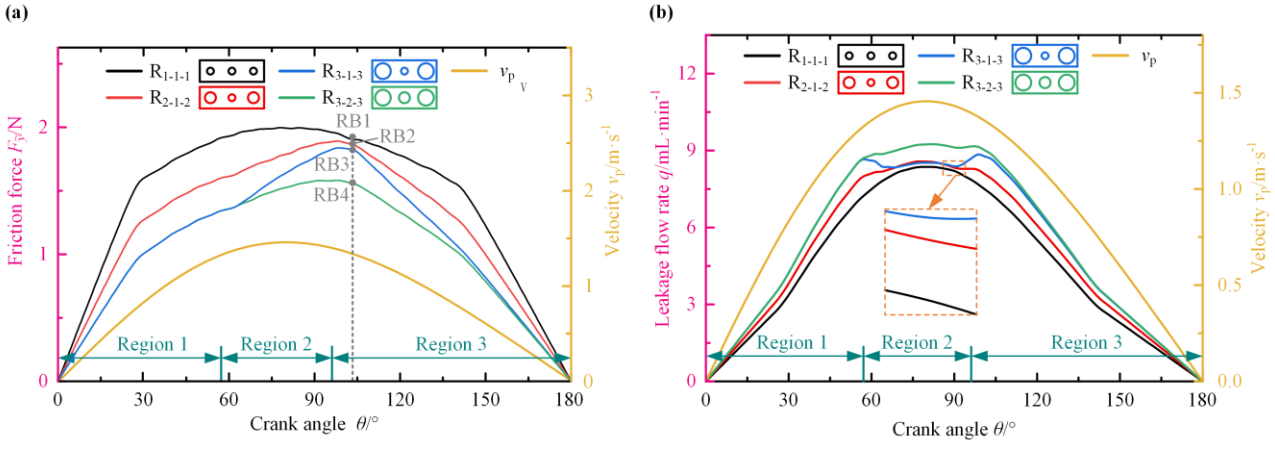


Figure 11. Friction force and leakage flow rate for DXD texture combinations: (a) friction force; (b) leakage flow rate.

Characteristic points RB1–RB4 were selected from the friction-force curves for pressure analysis. Fig. 12 shows the pressure contours at these points. The pressure peak increases from RB1 to RB2, decreases slightly at RB3 as the medium- and high-pressure regions expand, and remains nearly unchanged at RB4 as these regions expand further. Cavitation limits the influence of low-pressure region variations on the overall oil-film load-carrying capacity. Together with the friction force at each point in Fig. 11(a), the contours indicate that the oil-film load-carrying capacity increases from RB1 to RB4. Fig. 11(b) shows the leakage flow rate for the DXD texture combinations. The leakage flow rates of all DXD texture combinations are higher than that of the control group, and their overall half-cycle trends and inflection-point positions are similar to those of the XDX texture combinations. Comparison with Fig. 9(b) shows that, as the computational region moves from Region 1 into Region 2 and the texture radius changes, the leakage flow rate increases markedly for XDX but decreases for DXD.

The larger- and smaller-radius texture distributions in DXD are opposite to those in XDX. Accordingly, the friction force, characteristic-point pressure contours, and leakage flow rate show opposite trends despite similar underlying mechanisms.

https://doi.org/10.5194/ms-2026-210
Preprint. Discussion started: 26 November 2026
© Author(s) 2026. CC BY 4.0 License.

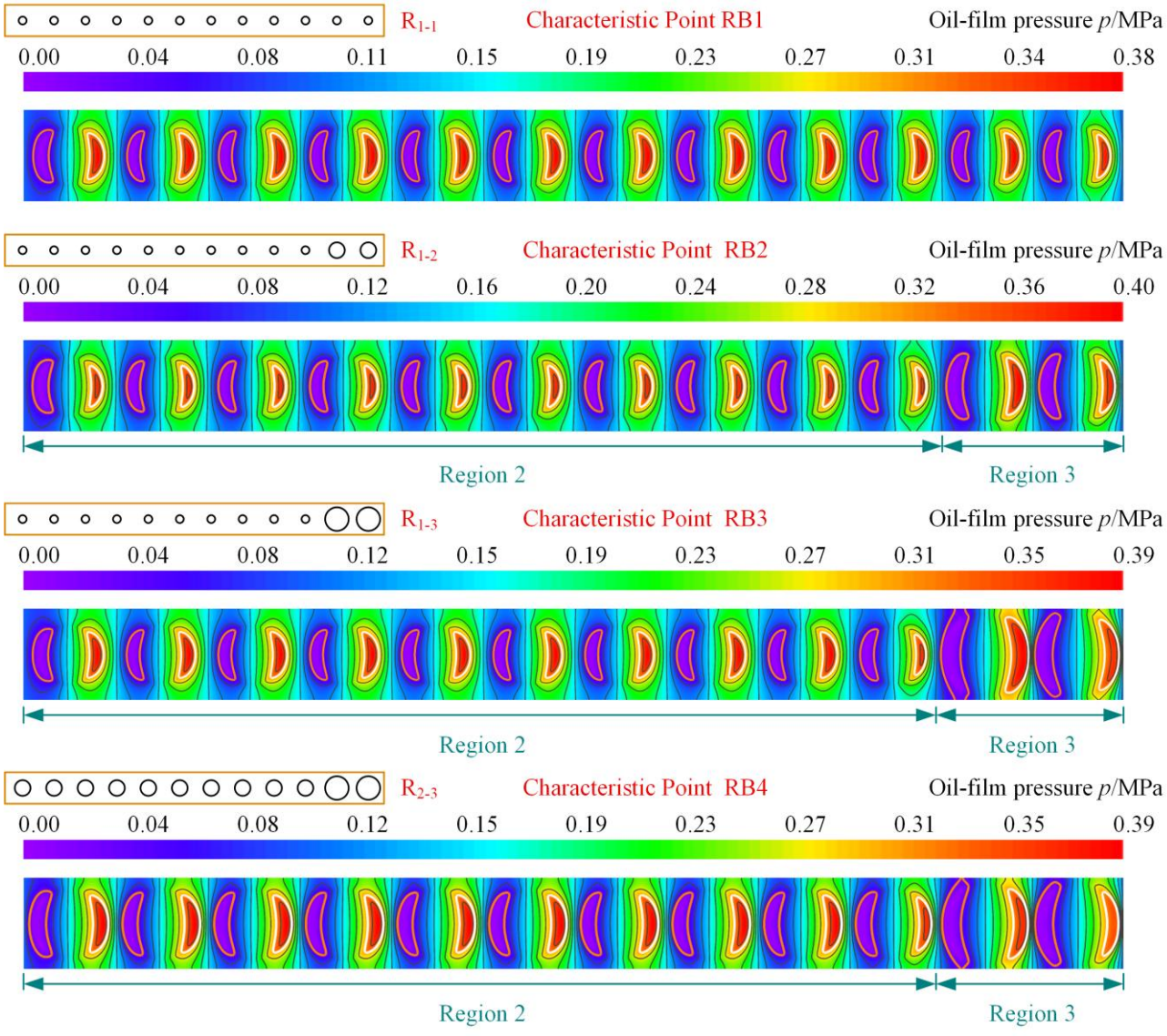
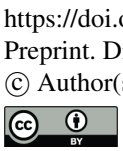


Figure 12. Pressure contours at characteristic points of the friction force curves for DXD texture combinations.

Fig. 13 shows the mean friction force and mean leakage flow rate for the texture-radius combinations. Compared with the control group, both XDX and DXD reduce the mean friction force but increase the mean leakage flow rate. Overall, XDX yields a lower mean leakage flow rate but a higher mean friction force than DXD. These differences mainly reflect the textured-area proportion within the computational region: a larger proportion increases the interconnected clearance between the friction-pair surfaces, improving lubrication and reducing the friction coefficient while increasing the leakage flow rate.

Compared with the control group, $R_{3\text{-}1\text{-}3}$ reduces the mean friction force by 21.3% but increases the mean leakage flow rate by 15.3%. $R_{3\text{-}1\text{-}3}$ and $R_{2\text{-}3\text{-}2}$ exhibit similar mean friction force and mean leakage flow rate. However, as shown in Figs. 9(a) and

https://doi.org/10.5194/ms-2026-210
Preprint. Discussion started: 26 November 2026
© Author(s) 2026. CC BY 4.0 License.



mechanical sciences DISCUSSIONS

11(a), $R_{2\text{-}3\text{-}2}$ exhibits a lower maximum friction force than $R_{3\text{-}1\text{-}3}$, making it more suitable for long-term operation.

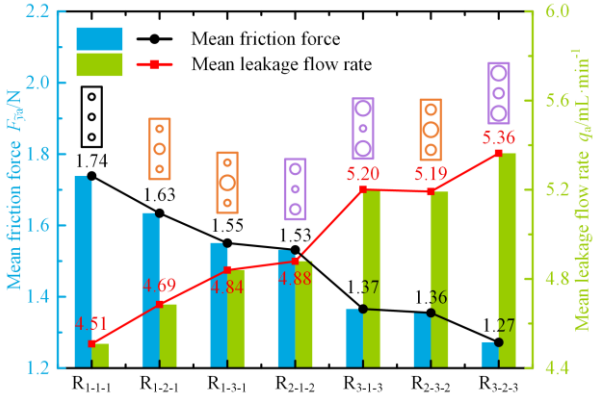


Figure 13. Mean friction force and mean leakage flow rate for texture-radius combinations.

5.3 Effect of Texture-Depth Combination

Figure 14 shows the friction force and leakage flow rate for the QSQ texture combinations. Figure 14(a) presents the friction force, whereas Fig. 14(b) presents the leakage flow rate. Over the half-cycle, the friction force generally follows piston velocity, first increasing and then decreasing, with nearly overlapping curves. Figure 15 shows the pressure contours at characteristic points DC1–DC4 selected for pressure analysis.

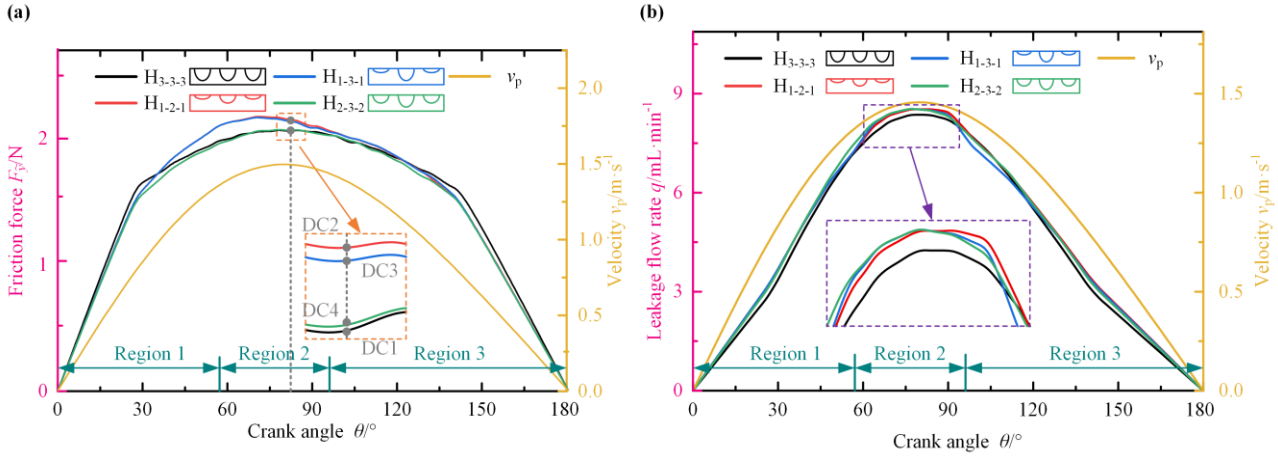


Figure 14. Friction force and leakage flow rate for QSQ texture combinations: (a) friction force; (b) leakage flow rate.

https://doi.org/10.5194/ms-2026-210
Preprint. Discussion started: 26 November 2026
© Author(s) 2026. CC BY 4.0 License.

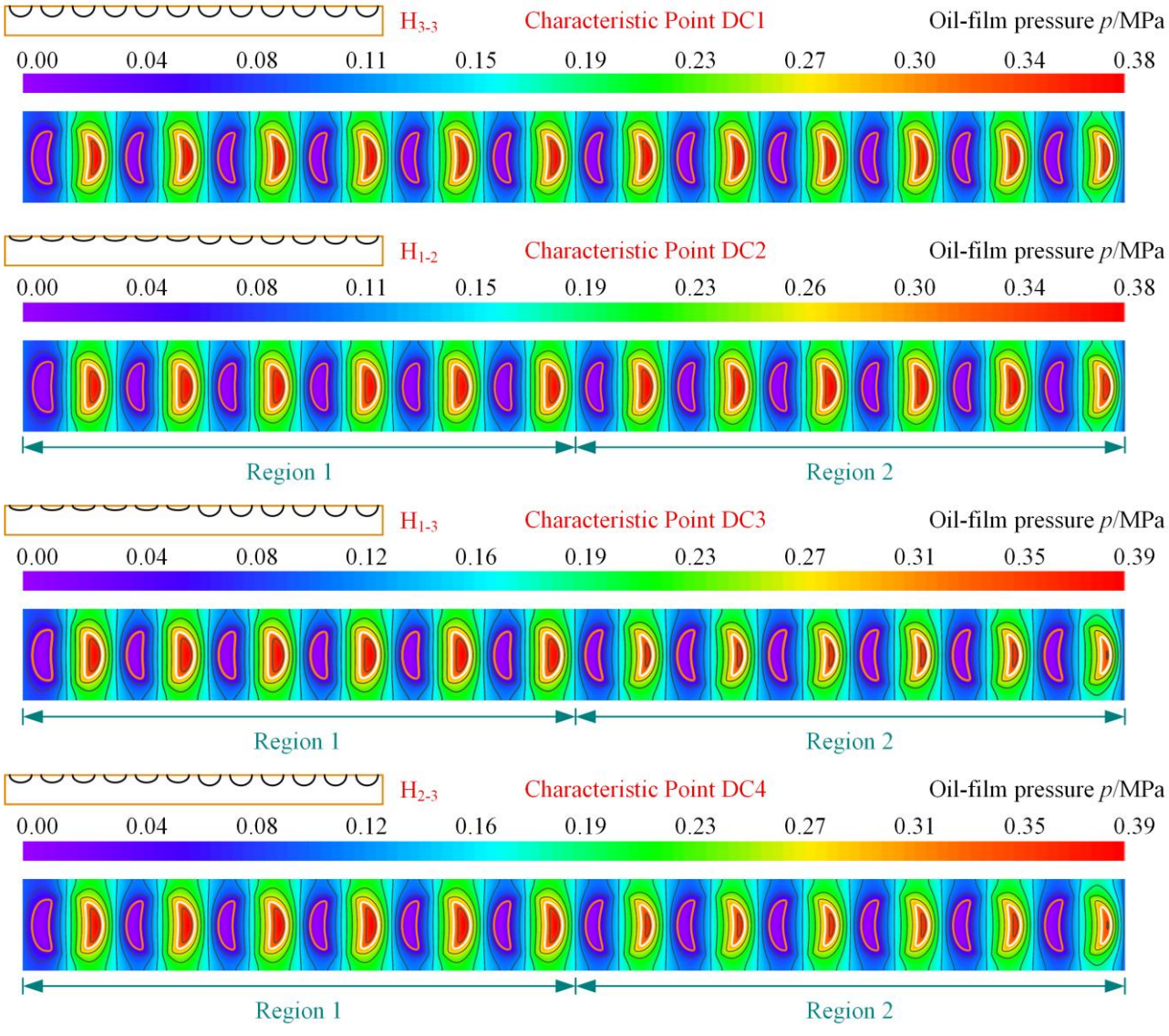


Figure 15. Pressure contours at characteristic points of the friction force curves for QSQ texture combinations.

DC1 and DC2 have different texture depths in Region 1 but the same depth in Region 2. Their maximum oil-film pressures and high- and low-pressure regions are nearly identical, while their friction forces differ only slightly, suggesting similar oil-film load-carrying capacities. DC2 and DC3 have the same texture depth in Region 1 but different depths in Region 2. Although DC3 exhibits slightly smaller medium- and high-pressure regions and a slightly higher pressure peak, their friction forces remain similar, indicating little difference in oil-film load-carrying capacity.

Overall, DC1–DC4 show only minor differences in peak oil-film pressure, pressure distribution, and friction force. Therefore, the oil-film load-carrying capacities of the different QSQ texture combinations are also expected to be similar.

https://doi.org/10.5194/ms-2026-210
Preprint. Discussion started: 26 November 2026
© Author(s) 2026. CC BY 4.0 License.



mechanical sciences DISCUSSIONS

Figure 14(b) shows the leakage flow rate for the QSQ texture combinations. Its overall variation generally follows the piston velocity, and only minor differences are observed among the combinations in Region 2.

Overall, the QSQ texture combinations exhibit only minor differences in friction force, oil-film pressure distribution, maximum oil-film pressure, and leakage flow rate. Because the QSQ configurations use relatively shallow textures, the lubrication performance of the piston pair is relatively insensitive to the texture-depth arrangement and to further increases in texture depth.

Figure 16 shows the friction force and leakage flow rate for the SQS texture combinations. As shown in Fig. 16(a), the friction force variation is similar to that of the QSQ texture combinations, with only minor differences among the curves. Characteristic points DD1–DD4 were selected for pressure analysis, and their pressure contours are shown in Fig. 17. Similar to the QSQ texture combinations, no obvious differences are observed in the maximum oil-film pressure or the high- and low-pressure core regions.

Figure 16(b) shows that the leakage flow rate of the SQS texture combinations follows a trend similar to that of the QSQ texture combinations in Fig. 14(b).

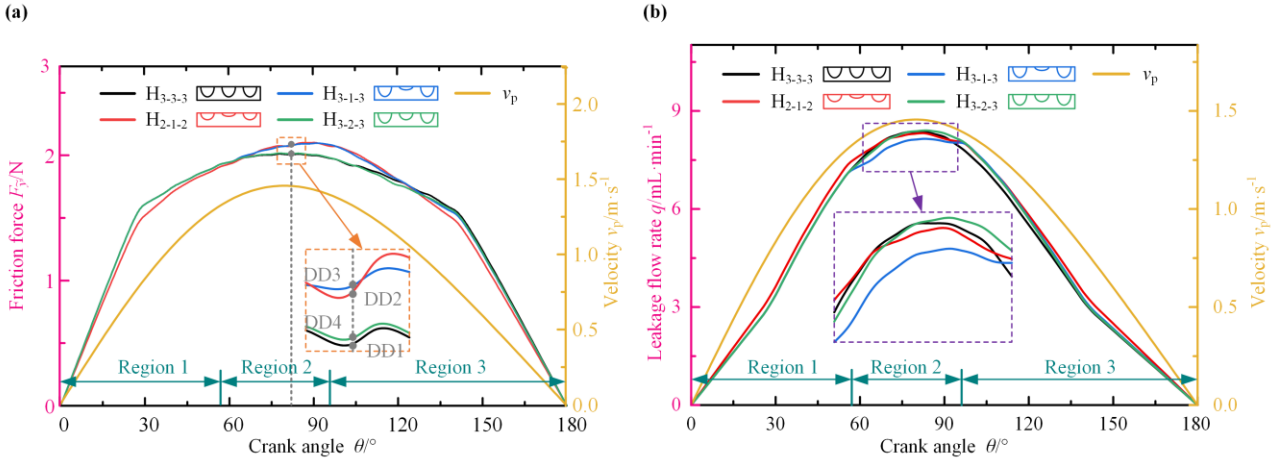


Figure 16. Friction force and leakage flow rate for SQS texture combinations: (a) friction force; (b) leakage flow rate.

https://doi.org/10.5194/ms-2026-210
Preprint. Discussion started: 26 November 2026
© Author(s) 2026. CC BY 4.0 License.

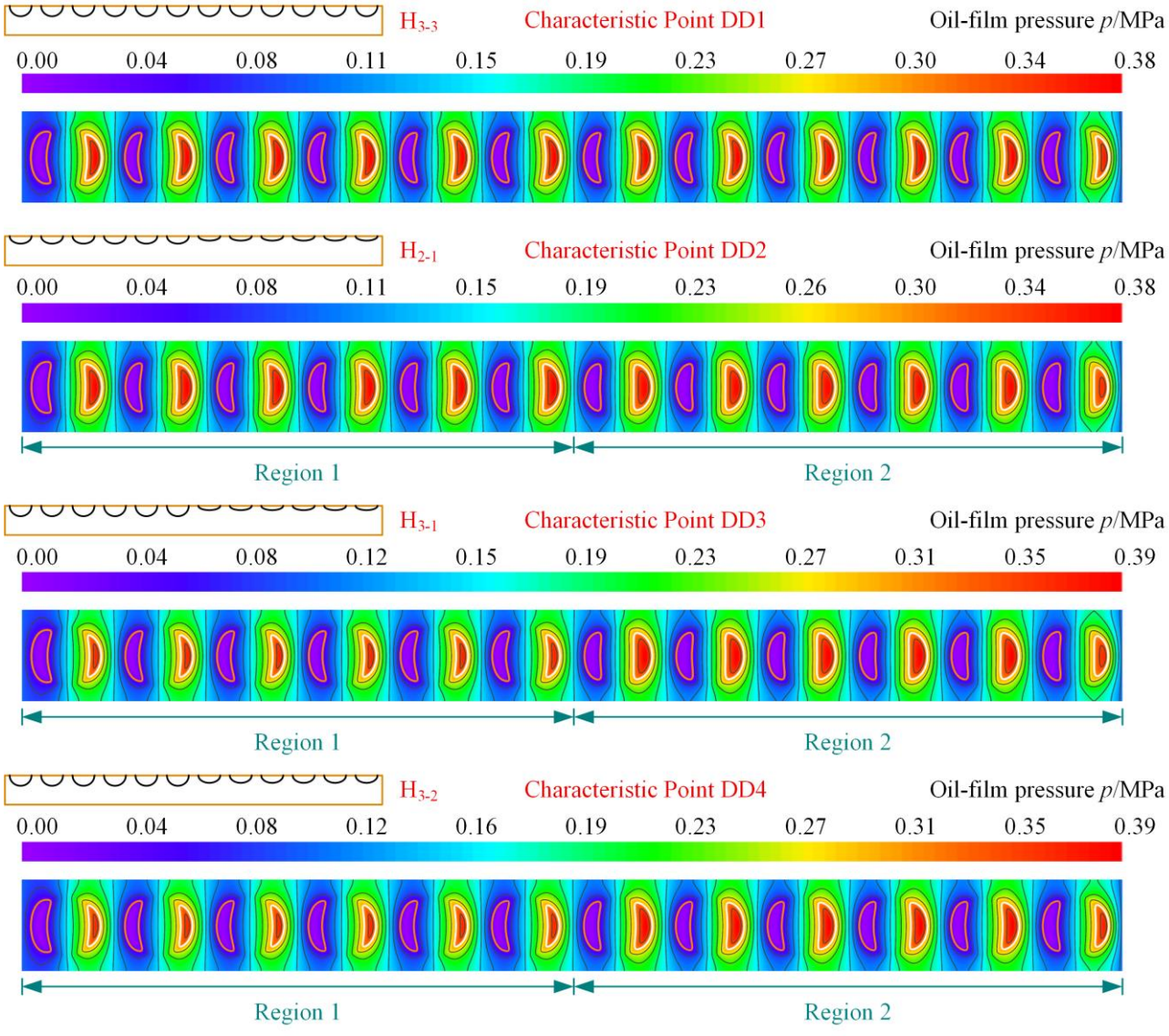


Figure 17. Pressure contours at characteristic points of the friction force curves for SQS texture combinations.

Figure 18 shows minor differences in mean friction force and mean leakage flow rate between the texture-depth combinations and control group, suggesting limited effects on piston pair lubrication performance under the simulated operating conditions.

https://doi.org/10.5194/ms-2026-210
Preprint. Discussion started: 26 November 2026
© Author(s) 2026. CC BY 4.0 License.

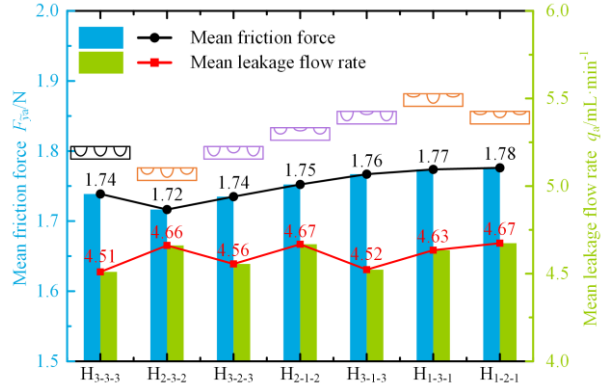
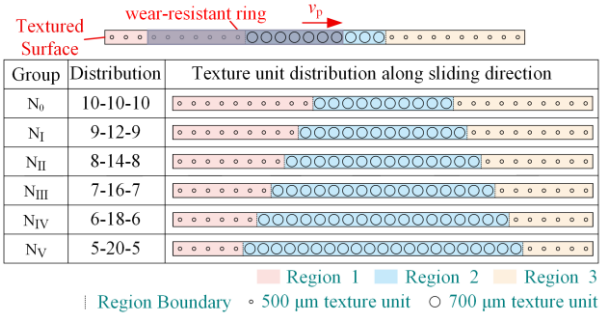


Figure 18. Mean friction force and mean leakage flow rate for texture-depth combinations.

5.4 Effect of Non-Uniform Texture Combinations

Figure 9(a) shows that XDX reduces the maximum friction force, with similar inflection-point positions near the region boundaries across texture radii, suggesting that the region arrangement may affect both. Given the favorable friction characteristics of Region 2, $R_{1\text{-}3\text{-}1}$ was selected for further investigation. As shown in Fig. 19, Region 2 was lengthened to increase its texture count while keeping the total number of texture units constant. Figure 20 shows the friction force and leakage flow rate for different non-uniform texture combinations.



Group	Distribution	Texture unit distribution along sliding direction
N_0	10-10-10	
N_I	9-12-9	
N_{II}	8-14-8	
N_{III}	7-16-7	
N_{IV}	6-18-6	
N_V	5-20-5	

Figure 19. Design parameters of non-uniform texture combinations.

https://doi.org/10.5194/ms-2026-210
Preprint. Discussion started: 26 November 2026
© Author(s) 2026. CC BY 4.0 License.

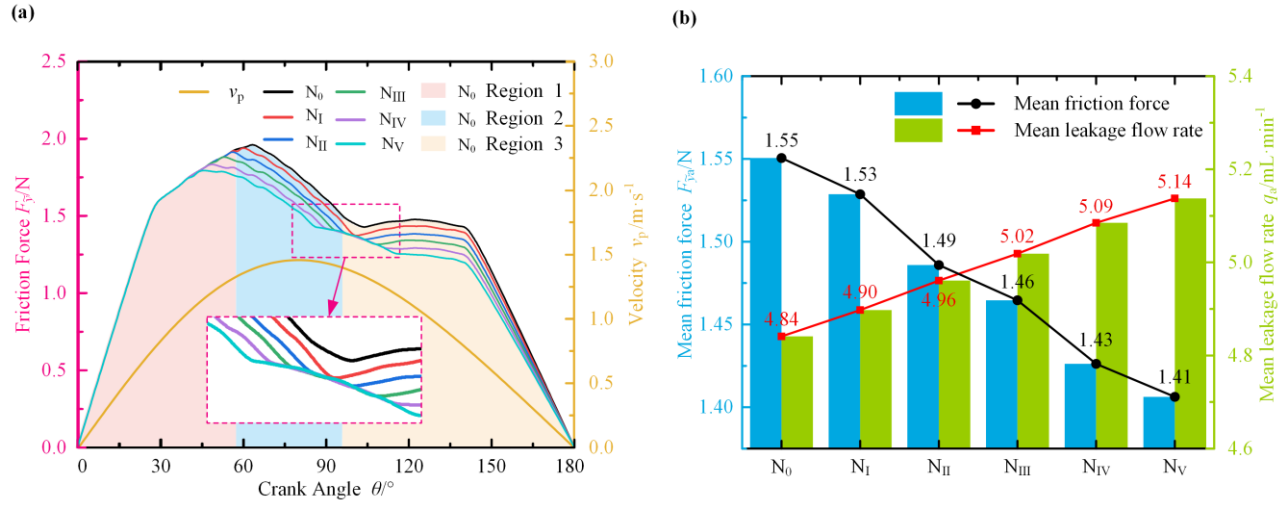


Figure 20. Effects of non-uniform texture-combination parameters on lubrication characteristics: (a) friction force under different non-uniform texture-combination parameters; (b) mean friction force and mean leakage flow rate under different texture-combination parameters.

In Fig. 20(a), lengthening Region 2 reduces the maximum friction force and extends the inflection-point region, with the maximum and inflection points near the boundaries of Regions 1–2 and Regions 2–3, respectively. Figure 20(b) shows that Group NV has the lowest mean friction force (9% lower) and highest mean leakage flow rate (5.8% higher) relative to the control group.

6 Reciprocating Friction and Wear Test

6.1 Experimental Design

Figure 21 shows the reciprocating friction and wear test setup and equivalent piston pair specimens. In Fig. 21(a), the motor reciprocates the upper specimen held in the upper fixture, while the lower specimen is fixed in the oil bath on the loading platform. The friction pair is fully immersed in lubricating oil. Figure 21(b) and Fig. 21(c) show the upper and lower specimens, respectively.

Simulations indicate that texture radius affects lubrication performance more strongly than texture depth. R1-1-1 specimens therefore served as the control group for evaluating texture radius and texture-radius combinations. All specimens had identical texture density and texture depth. Figure 22 shows the experimental texture configurations. Figure 22(a) shows the lower specimens with a single texture radius, whereas Fig. 22(b) shows those with different texture-radius combinations.

https://doi.org/10.5194/ms-2026-210
Preprint. Discussion started: 26 November 2026
© Author(s) 2026. CC BY 4.0 License.

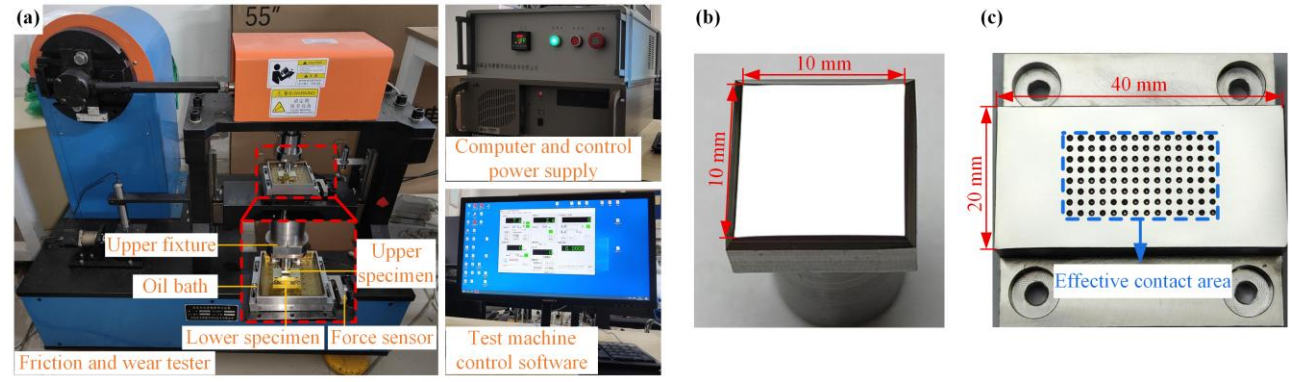


Figure 21. Reciprocating friction and wear test setup and equivalent specimens of the piston pair: (a) reciprocating friction and wear tester; (b) equivalent upper specimen of the piston pair; (c) equivalent lower specimen of the piston pair.

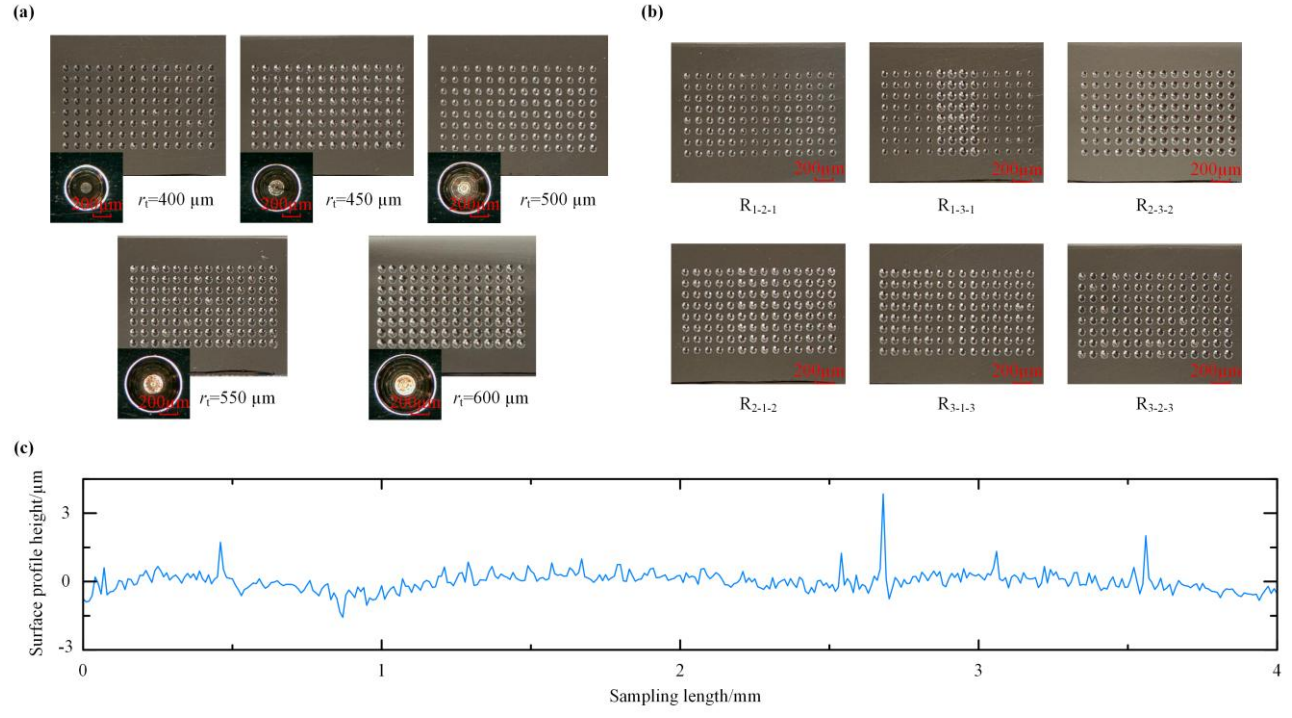


Figure 22. Surface textures of the lower specimens and surface roughness measurement: (a) lower specimen surface with a single texture radius; (b) lower specimen surfaces with different texture-radius combinations; (c) surface roughness measurement.

Reciprocating friction and wear tests were conducted under a 20 N load at a reciprocating frequency of 8 Hz, atmospheric pressure, and room temperature. A force sensor monitored friction force on the lower specimen in real time; the friction coefficient was calculated from this force and the load applied to the upper specimen. Each test was repeated five times to ensure reliability.

https://doi.org/10.5194/ms-2026-210
Preprint. Discussion started: 26 November 2026
© Author(s) 2026. CC BY 4.0 License.



mechanical sciences DISCUSSIONS

6.2 Effect of Texture Radius

Figure 23 shows the effects of texture radius and texture-radius combinations on friction characteristics. As shown in Fig. 23(a), the friction coefficient is generally highest at 400 μm and lowest at 600 μm. As shown in Fig. 23(b), the mean friction coefficient decreases with increasing texture radius, reaching a minimum of 0.107 at 600 μm. Under a constant applied load, the friction force trend agrees with the preceding simulations, supporting the reliability of the numerical model.

6.3 Effect of Texture-Radius Combination

As shown in Figs. 23(c) and 23(d), all texture-radius combinations yield lower friction coefficients than the control group throughout the test. Figure 23(e) shows that DXD generally exhibits a lower mean friction coefficient. The mean friction coefficient is similar for $R_{1\text{-}3\text{-}1}$, $R_{2\text{-}1\text{-}2}$, and $R_{3\text{-}1}$-3, but lowest for $R_{3\text{-}2\text{-}3}$, at 53.9% below $R_{1\text{-}1\text{-}1}$. The simulated mean friction force trend agrees well with the experimental mean friction coefficient trend, with $R_{3\text{-}2\text{-}3}$ also exhibiting the lowest mean friction force.

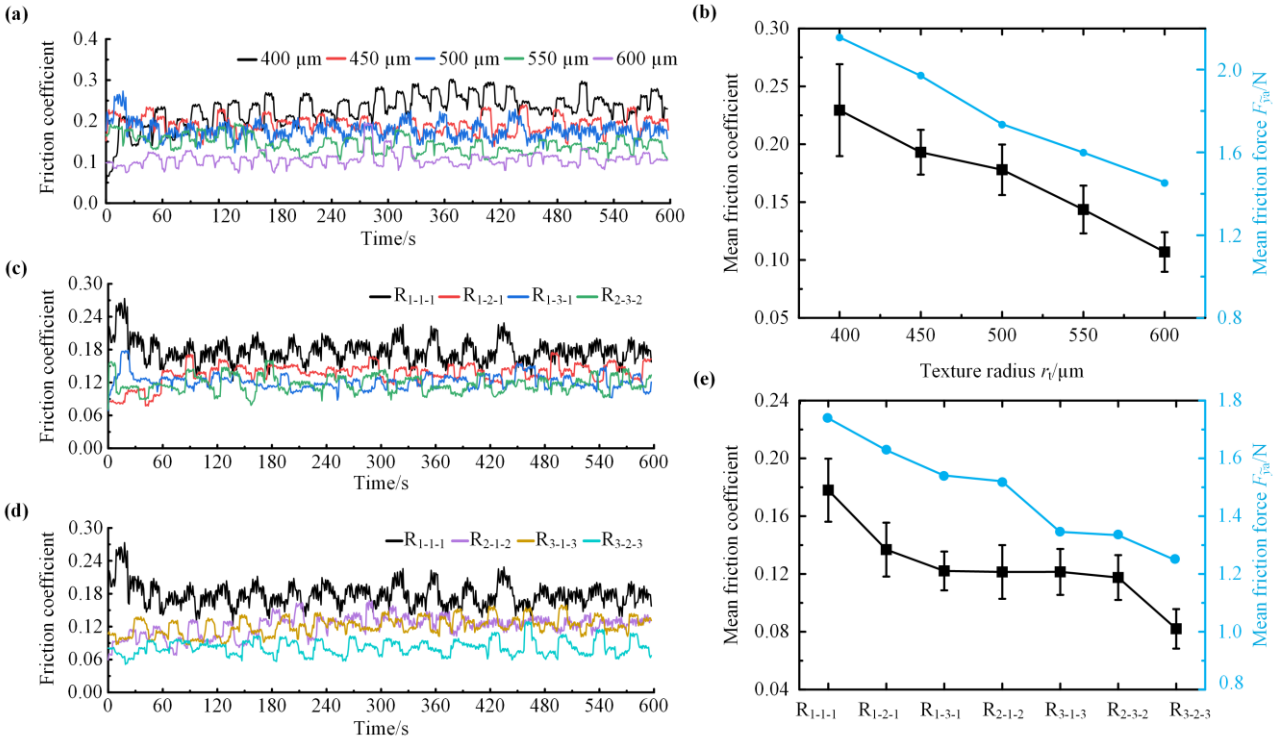


Figure 23. Effects of texture radius and texture-radius combinations on friction characteristics: (a) friction coefficient under different texture radii; (b) comparison of trends in mean friction coefficient and mean friction force under different texture radii; (c) friction coefficient for XDX texture combinations; (d) friction coefficient for DXD texture combinations; (e) comparison of trends in mean friction coefficient and mean friction force for different texture-radius combinations.

https://doi.org/10.5194/ms-2026-210
Preprint. Discussion started: 26 November 2026
© Author(s) 2026. CC BY 4.0 License.



mechanical sciences
DISCUSSIONS

7 Conclusions

A hydrodynamic lubrication model of a textured piston pair was established using the finite difference method to assess how texture geometry and combinations affect lubrication and friction-reduction performance. The main conclusions are:

(1) Under the simulated fluid-discharge condition, the friction force and leakage flow rate generally follow piston velocity, first increasing and then decreasing. Increasing texture radius or decreasing texture depth reduces the friction force and enhances the oil-film load-carrying capacity but increases the leakage flow rate. A spherical-cap texture with a radius of 500 μm and a depth of 20 μm provides favorable lubrication performance with a small increase in leakage flow rate.

(2) Lubrication performance is more sensitive to texture-radius combinations than texture-depth combinations. All texture-radius combinations yield lower friction force than the control group, with inflection points near the region boundaries. DXD generally exhibits lower friction force but higher leakage flow rate than XDX. Increasing the proportion of larger-radius textures enhances the oil-film load-carrying capacity and reduces the friction force but increases the leakage flow rate. $R_{2\text{-}3\text{-}2}$ shows favorable overall performance among uniformly divided combinations.

(3) The friction force extrema and inflection-point positions depend on region arrangement and piston velocity, with the maximum and inflection points near the region boundaries. Lengthening Region 2 increases the number of larger-radius textures, reduces the maximum friction force, shifts its position leftward, and extends the inflection-point region. Adjusting the boundaries of Region 2 can therefore regulate the friction force curve in non-uniform texture arrangements. Compared with the uniform arrangement, Group N_V reduces the mean friction force by 9% but increases the mean leakage flow rate by 5.8%.

(4) Experimental trends agree well with simulations. For specimens with a single texture radius, the mean friction coefficient decreases with increasing texture radius, reaching a minimum of 0.107 at 600 μm. Among texture-radius combinations, $R_{3\text{-}2\text{-}3}$ provides the best friction-reduction performance, with a mean friction coefficient 53.9% lower than that of the control group $R_{1\text{-}1\text{-}1}$.

Code and data availability

This study employed existing finite element simulation software in conjunction with MATLAB-based finite difference numerical programs. Programs implementing the finite difference method are available through existing resources. The numerical procedures, material models, boundary conditions, and analysis parameters are described in sufficient detail in this paper to ensure the reproducibility of the results.

The data supporting the findings of this study are not publicly available due to confidentiality requirements and institutional restrictions. These data are associated with ongoing research projects and therefore cannot be publicly released. However, the data may be obtained from the corresponding author upon reasonable request and with permission from the relevant parties

https://doi.org/10.5194/ms-2026-210
Preprint. Discussion started: 26 November 2026
© Author(s) 2026. CC BY 4.0 License.



mechanical sciences
DISCUSSIONS

Team list

Tao He[1,2,3],Qiao Zhang[1],Yunlong Gu[1],Gang Luo[1,2],Kaiping Zhao[2],Chuanli Wang[1,2,3]

[1]School of Mechatronics Engineering, Anhui University of Science and Technology, Huainan Anhui 232001, China

[2]State Key Laboratory of Digital Intelligent Technology for Unmanned Coal Mining, Anhui University of Science and Technology, Huainan Anhui 232001, China

Anhui Key Laboratory of Mine Intelligent Equipment and Technology, Anhui University of Science and Technology, Huainan Anhui 232001, China

Author contributions

TH supervised the overall research process, reviewed the manuscript, and provided funding support. QZ drafted, revised, and edited the manuscript. YG conducted the experiments and provided the original experimental data. GL supervised the experimental work. KZ provided guidance on manuscript revision and editing. CW, as the corresponding author, proposed the research topic and guided the overall research framework and direction. All authors reviewed and approved the final manuscript.

Competing interests

The authors declare that they have no conflict of interest.

Acknowledgements

The authors gratefully acknowledge the financial support provided by the National Natural Science Foundation of China (grant nos. 52675052 and 52205041).

Financial support

This work was supported by the National Natural Science Foundation of China (Grant No. 52675052 and 52205041).

References

Bao, Y., Wang, C., Jin, Z., Wu, X., and Bao, J.: Textured surface on a bioceramic coating via a femtosecond laser and its friction and wear properties (in Chinese), Chinese Journal of Lasers, 46(2), 0203003, https://doi.org/10.3788/CJL201946.0203003, 2019.

https://doi.org/10.5194/ms-2026-210
Preprint. Discussion started: 26 November 2026
© Author(s) 2026. CC BY 4.0 License.



mechanical sciences
DISCUSSIONS

Cheng, J., Chen, W., Li, D., Chen, H., Guo, S., Zhou, Y., Yuan, H., and Wei, B.: Effect of spherical crown texturing and ionized sulfur infiltration on the tribological performance of piston-cylinder liner, Tribol. Int., 189, 108969, https://doi.org/10.1016/j.triboint.2023.108969, 2023.

Fan, Y., Hao, M., Chen, Y., Xia, J., and Li, B.: Improvement of friction performance of cylinder liner surface with composite lubrication texture under fluid lubrication condition (in Chinese), Journal of Drainage and Irrigation Machinery Engineering, 41(12), 1290–1296, https://doi.org/10.3969/j.issn.1674-8530.23.0185, 2023.

Gao, T., Zhang, H., Xu, J., Ma, B., and Cong, Q.: Effects of cylindrical pit array on tribological property of piston–cylinder sleeve friction pair in a BW-250 slime pump, Tribol. Int., 151, 106505, https://doi.org/10.1016/j.triboint.2020.106505, 2020.

Gao, T., Wang, Y., Xie, B., Chen, T., Xu, J., Zhang, N., and Tang, D.: The testing and optimization of a bio-inspired textured piston for the BW-250 mud pump, Polym. Test., 130, 108296, https://doi.org/10.1016/j.polymertesting.2023.108296, 2024.

He, T., Chen, Q., Chen, G., Wang, C., Huang, S., and Shen, H.: Research on lubrication and bearing characteristics of variable texture on sliding friction pair surface (in Chinese), Chinese Journal of Engineering Design, 28(5), 585–593, https://doi.org/10.3785/j.issn.1006-754X.2021.00.079, 2021.

He, T., Zheng, H., Deng, H., Fang, S., Wang, C., and Luo, G.: Study on abrasive wear of textured slider friction pair of horizontal pump, Proceedings of the Institution of Mechanical Engineers, Part J: Journal of Engineering Tribology, 239(11), 1478–1493, https://doi.org/10.1177/13506501251319068, 2025.

He, T., Qian, Y., Deng, H., Luo, G., Wang, C., and Han, Y.: Effect of hybrid texture surface on the tribological properties of martensitic stainless steel (in Chinese), Tribology, accepted manuscript, online first, 3 June 2026, 2026.

Huang, P., et al.: Numerical calculation methods for elastohydrodynamic lubrication (in Chinese), Tsinghua University Press, Beijing, 2013.

Li, R.: Intelligent fluid supply technology in fully-mechanized coal mining face and its development trend (in Chinese), Coal Science and Technology, 47(9), 203–207, https://doi.org/10.13199/j.cnki.cst.2019.09.025, 2019.

Li, R., Ye, J., Lu, H., Lai, Y., Liu, H., Chen, R., Yu, T., Kang, Y., Wang, C., and Wang, D.: Research on key technology and engineering application of emulsion pump in super-high mining face (in Chinese), Coal Science and Technology, 52(11), 153–162, https://doi.org/10.12438/cst.2024-1019, 2024.

Li, X., Geng, Z., Su, X., Tang, J., Chen, J., and Shao, W.: Numerical simulation and experimental investigation of mixed thermal elastohydrodynamic lubrication in point contact with droplet-shaped composite textured surfaces, Tribol. Int., 215, 111448, https://doi.org/10.1016/j.triboint.2025.111448, 2026.

Li, Y., Zhang, Z., He, Y., and Luo, J.: Optimization of surface texture distribution on the thrust bearing using the mass-conserving cavitation boundary condition: theory and experiments, Tribol. Int., 194, 109551, https://doi.org/10.1016/j.triboint.2024.109551, 2024.

https://doi.org/10.5194/ms-2026-210
Preprint. Discussion started: 26 November 2026
© Author(s) 2026. CC BY 4.0 License.



Liang, Y., Xing, H., Li, X., Wang, H., Li, Y., Liang, X., Zhang, F., Chen, N., Zhou, Y., and Gao, D.: Investigation on the coupling mechanism of lubrication characteristics and wear evolution in axial piston pump slippers based on surface texture: a fluid–solid–thermal coupled analysis, Eng. Fail. Anal., 195, 111020, https://doi.org/10.1016/j.engfailanal.2026.111020, 2026.

Liu, W., Tan, Z., Chen, W., Dai, Y., Yuan, H., Cheng, J., Wei, B., and Zhou, Y.: Research status and development trend of piston ring material and surface treatment technology for internal combustion engine (in Chinese), Surface Technology, 53(12), 36–49, https://doi.org/10.16490/j.cnki.issn.1001-3660.2024.12.003, 2024.

Liu, W., Zhang, W., Hu, Z., Tang, J., Zhou, Y., Yin, F., Zhou, Z., and Wang, Z.: Transient mixed thermo-elastohydrodynamic lubrication of surface micro-textured face gear pair, Tribol. Int., 217, 111680, https://doi.org/10.1016/j.triboint.2026.111680, 2026.

Liu, Y.: The fundamentals of water hydraulics and its engineering applications (in Chinese), Mechanical Industry Press, Beijing, 2013.

Liu, Y., Dong, J., Wei, W., Zhao, S., Li, R., Liu, H., Ye, J., and Wu, D.: Research status and green development trend and prospect of mine high-power plunger pump (in Chinese), Journal of Mechanical Engineering, 59(10), 333–345, https://doi.org/10.3901/JME.2023.10.333, 2023.

Lu, J.: Study on improving the friction performance of axial piston surfaces by laser-ablated microtextures (in Chinese), M.S. thesis, Jiangsu University of Science and Technology, Zhenjiang, 2022.

Luo, G., He, T., Wang, C., and Zhao, K.: Research on lubrication characteristics of textured piston-cylinder pairs in axial piston pumps during the low-pressure stroke (in Chinese), China Mechanical Engineering, 36(11), 2525–2536, https://doi.org/10.3969/j.issn.1004-132X.2025.11.007, 2025.

Ma, J., Liu, Y., Yi, P., Jia, H., Zhang, N., and Sun, J.: Anti-friction mechanism of sinusoidal texture with various intervals: the synergistic effect of dynamic pressure and tribofilm, Tribol. Int., 173, 107635, https://doi.org/10.1016/j.triboint.2022.107635, 2022.

Mishra, P. and Penchaliah, R.: Synergistic effect of surface texturing and coating on the friction between piston ring and cylinder liner contact, Proceedings of the Institution of Mechanical Engineers, Part J: Journal of Engineering Tribology, 235(7), 1298–1311, https://doi.org/10.1177/1350650120951289, 2021.

Niu, Q., Zhu, C., Wu, B., Zhang, S., Guo, T., and Gao, J.: Research progresses on synergistic technology of micro-textured and minimum quantity lubrication on tool surfaces (in Chinese), China Mechanical Engineering, 37(4), 885–899, https://doi.org/10.3969/j.issn.1004-132X.2026.04.013, 2026.

Pawlus, P. and Reizer, R.: Functional importance of honed cylinder liner surface texture: a review, Tribol. Int., 167, 107409, https://doi.org/10.1016/j.triboint.2021.107409, 2022.

Profito, F. J., Vladescu, S.-C., Reddyhoff, T., and Dini, D.: Numerical and experimental investigation of textured journal bearings for friction reduction, Tribol. Int., 195, 109643, https://doi.org/10.1016/j.triboint.2024.109643, 2024.

https://doi.org/10.5194/ms-2026-210
Preprint. Discussion started: 26 November 2026
© Author(s) 2026. CC BY 4.0 License.



mechanical sciences
DISCUSSIONS

Qin, S., Shi, X., Huang, Y., Zhang, K., Huang, Q., and Wu, C.: Interface characteristics of textured composite solid lubricant coating to improve the tribological performance of TC4, Friction, 13(5), 9440942, https://doi.org/10.26599/FRICT.2025.9440942, 2025.

Wang, B., Qian, S., Wang, H., Du, X., and Chen, X.: Cavitation effect on tribological performance of journal bearing with asymmetric micro-texture (in Chinese), Surface Technology, 54(1), 171–180, https://doi.org/10.16490/j.cnki.issn.1001-3660.2025.01.016, 2025.

Wang, G., Liao, W., and Zhao, M.: Simulation analysis on hydrodynamic lubrication performance of fracturing pumper plunger seal with compound texture (in Chinese), Lubrication Engineering, 44(1), 20–30, https://doi.org/10.3969/j.issn.0254-0150.2019.01.004, 2019.

Wang, H., Lin, N., Yuan, S., Liu, Z., Yu, Y., Zeng, Q., Fan, J., Li, D., and Wu, Y.: Structural improvement, material selection and surface treatment for improved tribological performance of friction pairs in axial piston pumps: a review, Tribol. Int., 198, 109838, https://doi.org/10.1016/j.triboint.2024.109838, 2024.

Wang, L., Zhang, W., Ge, X., and Duan, J.: Effect of compound micro texture arrangement on journal bearing lubrication performance (in Chinese), China Surface Engineering, 36(1), 145–155, https://doi.org/10.11933/j.issn.1007-9289.20220502001, 2023.

Wang, Z., Hu, S., Ji, H., Wang, Z., and Liu, X.: Analysis of lubricating characteristics of valve plate pair of a piston pump, Tribol. Int., 126, 49–64, https://doi.org/10.1016/j.triboint.2018.05.008, 2018a.

Wang, Z., Hu, S., Zhang, H., Ji, H., Yang, J., and Liang, W.: Effect of surface texturing parameters on the lubrication characteristics of an axial piston pump valve plate, Lubricants, 6(2), 49, https://doi.org/10.3390/lubricants6020049, 2018b.

Wu, Y., Xi, W., Li, A., Han, L., and Zhang, M.: Heteromorphic texturization design and parameters optimization for gas journal microbearings (in Chinese), China Surface Engineering, 39(4), 204–219, https://doi.org/10.11933/CSE2026318, 2026.

Yang, W., Wang, J., Wang, X., and Chen, P.: Anisotropic tribology and electrification properties of sliding-mode triboelectric nanogenerator with groove textures, Friction, 12(8), 1828–1837, https://doi.org/10.1007/s40544-024-0861-z, 2024.

Yin, H., Chen, J., Guo, F., and Yang, J.: Surrogate-assisted multi-objective optimization of leaf-vein textured journal bearings under thermohydrodynamic lubrication, Tribol. Int., 220, 111936, https://doi.org/10.1016/j.triboint.2026.111936, 2026.

Yu, Y., Zhang, W., Wang, Z., Shen, J., and Ruan, W.: Multi-objective optimization and performance analysis of special-shaped micro-textures for cylindrical roller bearing (in Chinese), Lubrication Engineering, online first, 14 May 2026, https://link.cnki.net/urlid/44.1260.TH.20260514.0846.006, 2026.

Zhang, J., Lyu, F., Xu, B., Huang, W., Wu, W., Guo, Z., Xu, H., and Huang, X.: Simulation and experimental investigation on low wear rate surface contour of piston/cylinder pair in an axial piston pump, Tribol. Int., 162, 107127, https://doi.org/10.1016/j.triboint.2021.107127, 2021.

Zhang, Y. and Chen, S.: The influence of surface texture on three-lobe journal bearing (in Chinese), Manufacturing Technology & Machine Tool, no. 2, 125–130, https://doi.org/10.19287/j.cnki.1005-2402.2021.02.025, 2021.

https://doi.org/10.5194/ms-2026-210
Preprint. Discussion started: 26 November 2026
© Author(s) 2026. CC BY 4.0 License.



mechanical sciences
DISCUSSIONS

Zhu, C., Jiang, F., Xiong, J., Yang, F., and Li, Y.: Design and field test of surface-textured laser-cladded coatings for rotary tillage blades (in Chinese), Surface Technology, 55(11), 97–109, https://doi.org/10.16490/j.cnki.issn.1001-3660.2026.11.009, 2026.